Weighted Low-Rank Tensor Recovery for Hyperspectral Image Restoration

Yi Chang, *Student Member, IEEE*, Luxin Yan, *Member, IEEE*, Xi-Le Zhao, Houzhang Fang, Zhijun Zhang, and Sheng Zhong

***Abstract*—Hyperspectral imaging, providing abundant spatial and spectral information simultaneously, has attracted a lot of interest in recent years. Unfortunately, due to the hardware limitations, the hyperspectral image (HSI) is vulnerable to various degradations, such as noises (random noise), blurs (Gaussian and uniform blur), and downsampled (both spectral and spatial downsample), each corresponding to the HSI denoising, deblurring, and super-resolution tasks, respectively. Previous HSI restoration methods are designed for one specific task only. Besides, most of them start from the 1-D vector or 2-D matrix models and cannot fully exploit the structurally spectral–spatial correlation in 3-D HSI. To overcome these limitations, in this article, we propose a unified low-rank tensor recovery model for comprehensive HSI restoration tasks, in which nonlocal similarity within spectral–spatial cubic and spectral correlation are simultaneously captured by third-order tensors. Furthermore, to improve the capability and flexibility, we formulate it as a weighted low-rank tensor recovery (WLRTR) model by treating the singular values differently. We demonstrate the reweighed strategy, which has been extensively studied in the matrix, also greatly benefits the tensor modeling. We also consider the stripe noise in HSI as the sparse error by extending WLRTR to robust principal component analysis (WLRTR-RPCA). Extensive experiments demonstrate the proposed WLRTR models consistently outperform state-of-the-art methods in typical HSI low-level vision tasks, including denoising, destriping, deblurring, and super-resolution.**

***Index Terms*—Higher order singular value decomposition, hyperspectral image (HSI) restoration, low-rank tensor approximation (LRTA).**

Manuscript received September 12, 2019; revised January 9, 2020; accepted March 2, 2020. Date of publication April 23, 2020; date of current version October 26, 2020. This work was supported in part by the National Natural Science Foundation of China under Grant 61571207, Grant 61433007, Grant 41501371, and Grant 61876203, and in part by the Hubei Provincial Natural Science Foundation of China under Grant 2018CFA089. This article was recommended by Associate Editor S. Cruces. *(Corresponding author: Luxin Yan.)*

Yi Chang is with the National Key Laboratory of Science and Technology on Multispectral Information Processing, School of Artificial Intelligence and Automation, Huazhong University of Science and Technology, Wuhan 430074, China, and also with the Artificial Intelligent Center, Peng Cheng Laboratory, Shenzhen 518055, China (e-mail: yichang@hust.edu.cn).

Luxin Yan, Zhijun Zhang, and Sheng Zhong are with the National Key Laboratory of Science and Technology on Multispectral Information Processing, School of Artificial Intelligence and Automation, Huazhong University of Science and Technology, Wuhan 430074, China (e-mail: yanluxin@hust.edu.cn; zhijunzhang@hust.edu.cn; zhongsheng@hust.edu.cn).

Xi-Le Zhao is with the School of Mathematical Sciences, University of Electronic Science and Technology of China, Chengdu 611731, China (e-mail: xlzhao122003@163.com).

Houzhang Fang is with the School of Software, Xidian University, Xi'an 710071, China (e-mail: houzhangfang@xidian.edu.cn).

This article has supplementary downloadable material available at http://ieeexplore.ieee.org, provided by the authors.

Color versions of one or more of the figures in this article are available online at http://ieeexplore.ieee.org.

Digital Object Identifier 10.1109/TCYB.2020.2983102

I. Introduction

THE HYPERSPECTRAL image (HSI) consists of multiple discrete bands at specific frequencies. The HSI can deliver additional information that the human eye fails to capture for real scenes and has been attracting a lot of interest for researchers from a wide range of application fields, such as anomaly detection [1] and classification [2]. However, HSI always suffers from various degradations, such as random noise (caused by photon effects), stripe noise (due to calibration error between adjacent detectors), blur (on account of atmospheric turbulence or system motion), and low spatial resolution (because of hardware limitations). It is economically unsustainable and impractical to improve the HSI quality merely by the hardware scheme. Therefore, it is natural to introduce the image processing-based approaches for obtaining a high-quality HSI before the subsequent applications. Mathematically, the problem of HSI restoration can be formulated by a linear model as follows:

$$\mathcal{Y} = \mathcal{T}_{sa}(\mathcal{X}) + \mathcal{E} + \mathcal{N} \tag{1}$$

where $\mathcal{Y} \in \mathbb{R}^{r\times c\times B}$ is an observed low spatial-resolution image, $\mathcal{X} \in \mathbb{R}^{R\times C\times B}$ $(r \ll R, c \ll C)$ represents the original high spatial-resolution image, $\mathcal{E} \in \mathbb{R}^{r\times c\times B}$ denotes the sparse error (mainly the stripe noise), $\mathcal{N} \in \mathbb{R}^{r\times c\times B}$ means the additive random noise, and $\mathcal{T}_{sa}(\bullet)$ stands for the spatially linear degradation operator.

With different settings, (1) can represent different HSI restoration problems. When $\mathcal{T}_{sa}(\bullet)$ is an identity tensor, the problem (1) becomes HSI denoising (only consider $\mathcal{N}$) or HSI destriping (only consider $\mathcal{E}$), or HSI mixed noise removal (both $\mathcal{N}$ and $\mathcal{E}$); when $\mathcal{T}_{sa}(\bullet)$ is a blur operator, the problem (1) turns into the HSI deblurring; for HSI super-resolution, $\mathcal{T}_{sa}(\bullet)$ is a composite operator of blurring and spatial down sampling. Moreover, in HSI super-resolution, there is another guided low spectral-resolution multispectral image $\mathcal{Z} \in \mathbb{R}^{R\times C\times b}$ $(b \ll B)$ (usually RGB color image), which can be formulated as follows:

$$\mathcal{Z} = \mathcal{T}_{se}(\mathcal{X}) + \mathcal{N} \tag{2}$$

where $\mathcal{T}_{se}(\bullet)$ denotes a spectral downsampling procedure, which can be expressed as $\mathcal{X}\times_3 \boldsymbol{P}$, and $\boldsymbol{P} \in \mathbb{R}^{b\times B}$ is a transformation matrix mapping the HSI $\mathcal{X} \in \mathbb{R}^{R\times C\times B}$ to its RGB

2168-2267 © 2020 IEEE. Personal use is permitted, but republication/redistribution requires IEEE permission.
See https://www.ieee.org/publications/rights/index.html for more information.

Authorized licensed use limited to: XIDIAN UNIVERSITY. Downloaded on August 13,2026 at 11:06:50 UTC from IEEE Xplore. Restrictions apply.

representation $\boldsymbol{\mathcal{Z}} \in \mathbb{R}^{R\times C\times b}$ ($b \ll B$). The tensor product is defined in Section II.

To cope with the ill-posed nature of the HSI restoration task, various prior knowledge of the HSI is proposed to regularize the solution space

$$\min_{\boldsymbol{\mathcal{X}}} \frac{1}{2}\|\boldsymbol{\mathcal{Y}} - \mathcal{T}_{sa}(\boldsymbol{\mathcal{X}}) - \boldsymbol{\mathcal{E}}\|_F^2 + \frac{1}{2}\|\boldsymbol{\mathcal{Z}} - \mathcal{T}_{se}(\boldsymbol{\mathcal{X}})\|_F^2 + \lambda\Phi(\boldsymbol{\mathcal{X}}) \quad (3)$$

where $\|\bullet\|_F^2$ stands for the Frobenius norm; the first two data fidelity terms represent the spatial and spectral degradation process, respectively; $\Phi(\boldsymbol{\mathcal{X}})$ is a regularization term to enforce the solution with desired property; and λ is a tradeoff regularization parameter. The success of the HSI restoration heavily depends on how we choose proper prior knowledge. From the perspective of the data format in the prior, we classify the existing HSI restoration methods into three categories: 1) 1-D vector-based sparse representation methods [3]–[8]; 2) 2-D matrix-based low-rank matrix recovery (LRMR) methods [9]–[18]; and 3) 3-D tensor-based approximation methods [19]–[31].

Although the existing works have made significant progresses in HSI restoration, there are three main drawbacks to be improved. First, transforming the multidimensional HSI data into a vector or matrix usually breaks the spectral–spatial structural correlation. The recent works [25], [32] consistently indicate that the tensor-based methods substantially preserve the intrinsic structure correlation with better restoration results. Besides, some tensor-based methods are quite heuristic without taking the sparsity prior to consideration, which makes them hard to extend to other HSI restoration tasks. Second, compared with natural 2-D images, the HSI data could provide us extra spectral information. Unfortunately, many HSI restoration methods fall into the "trap" of high spectral correlation, while ignoring the nonlocal similarity [14], and vice-versa [32]. Thus, the results of these approaches may be suboptimal. Finally, most of the previous methods only employ the conventional $\boldsymbol{L}_1$ or nuclear norm as the sparsity constraint for HSI restoration. As a result, each patch is encoded equally. Such a mechanism may not take advantage of the structural difference of the image patch sufficiently.

In this article, to overcome the aforementioned drawbacks, we present a unified HSI restoration framework via the weighted low-rank tensor recovery (WLRTR) model. The tensor format naturally offers a unified understanding of the vector/matrix-based recovery models. Compared with the state-of-the-art HSI restoration methods, the contributions are as follows.

1) We propose a WLRTR model for HSI restoration, where the singular values in the core tensor are of different importance and assigned different weights. The simple yet effective weighted operation has an immediate physical interpretation, which has been extensively studied in the matrix. We demonstrate that the weighted strategy could be well extended to the tensor and facilitates HSI modeling.
2) Most of the HSI restoration methods encode the spectral or spatial information independently, and ignore the spatial-spectral structural correlation. Our method employs the low-rank tensor prior to modeling the spatial nonlocal self-similarity and spectral correlation property simultaneously, better preserving the intrinsic spectral–spatial structural correlation. Moreover, we extend WLRTR to the WLRT-RRPCA for sparse error modeling.
3) To the best of our knowledge, this is the first work that *comprehensively* considers the HSI restoration in a unified model. We validate WLRTR on several representative HSI restoration tasks, such as denoising, destriping, deblurring, and super-resolution, and the proposed WLRTR model consistently outperforms the state-of-the-art methods by a large margin. Furthermore, we show that the WLRTR can be well applied to multispectral images.

The related HSI restoration methods are introduced in Section II. Section III presents the WLRTR modeling and analyzes its closed-form solution. Section IV proposes the concrete objective function of each individual HSI restoration task and gives the corresponding optimization procedures. Extensive experimental results are reported in Section V. Section VI concludes this article.

II. Related Work

Low-Rank Modeling: The low-rank models have been extensively studied in HSI restorations [9]–[12], [14]–[17], [19]–[27]. The 2-D LRMR methods have shown great effectiveness to discover intrinsic low-dimensional structures in the high-dimensional HSI data. Zhang *et al.* [10], by lexicographically ordering the 3-D cube into a 2-D matrix representation along the spectral dimension, proposed a low-rank matrix restoration model for mixed noise removal in HSI. A lot of works follow this research line [11], [12], [14], [15], [18]. To better preserve the spatial-spectral correlation, the low-rank tensors recovery methods have been proposed [21]–[31]. Previous tensor-based methods equally treat each core tensor coefficient, ignoring the fact that each coefficient represents the different correlations across each mode. The reweighting strategy interprets the fine-grained structural discrepancy, and has been proven effective in vector/matrix cases [33], [34], while it has received less attention in tensor-based HSI restorations. In this article, we further take the fine-grained intrinsic sparsity of the core tensor into consideration via a reweighting strategy in order to better encode the structure correlation.

HSI Denoising: Image denoising is a test bed for various techniques. Consequently, numerous approaches for HSI denoising have been proposed [35]–[37]. The spectral correlation and nonlocal self-similarity are two kinds of intrinsic characteristics underlying an HSI. Most previous HSI denoising methods focus on the spectral correlation, such as the wavelet methods [4]; total variational methods [8]; the LRMR methods [10], [11], [14], [38]; or the nonlocal self-similarity, such as block-matching and 4-D filtering (BM4D) [39] and higher order SVD (HOSVD) [40] individually. Recently, Peng *et al.* [23] first modeled them simultaneously in tensor format. However, the tensor dictionary learning (TDL) [23] is quite heuristic and short of a concise formulation and, thus,

Authorized licensed use limited to: XIDIAN UNIVERSITY. Downloaded on August 13,2026 at 11:06:50 UTC from IEEE Xplore. Restrictions apply.

lacks the flexibility to other HSI restoration tasks. Several tensor works [24]–[27] follow the research line of [23] and model the sparsity of the core tensor in a principled manner. Interested readers could refer to [15] for a detailed background of HSI denoising.

HSI Destriping: Stripe noise is a very common structural noise in HSI. Traditional HSI destriping methods [10], [41]–[44] treated this problem as a denoising task and estimated the image directly with the white Gaussian noise assumption. Furthermore, Cao *et al.* [38] and Meng and De La Torre [45] held the point that the stripe line is a kind of structural noise and introduced the mixture of Gaussians (MoG) noise assumption to accommodate the stripe noise characteristic. On the contrary, some works started in the opposite direction by estimating the stripe noise only [46]–[48]. These methods regarded the stripe noise as a kind of specific image structure with fewer variables and regular patterns which makes the problem easier to solve. Our recent work [17] proposed treating the HSI destriping task as an image decomposition task, in which the clear image and stripe components were treated equally and estimated iteratively. Most of the previous methods are 2-D-based methods, failing to capture the spectral coherence. Compared with tensor-based RPCA methods [49], [50], our method further takes the structurally directional property of the sparse error into consideration. For the first time, we introduce the $\boldsymbol{L}_{211}$ norm (Section IV-B) into the tensor RPCA for structural stripe noise removal. Interested readers could refer to [17] for details.

HSI Deblurring: Natural image deblurring aims to recover a sharp latent image from a blurred one [51], which is a classical and active research field within the last decade. Numerous HSI deblurring methods directly learn natural image priors by assuming the widely used sparsity of image gradients, for example, Huber–Markov prior [52], the total variation (TV) [53], and the Gaussian mixture model (GMM) [54]. Only recently, the spatial-spectral joint TV has been introduced to HSI deblurring [55], [56]. In general, most previous HSI deblurring methods only exploit the spatial information, while none of them have utilized the nonlocal self-similarity property in HSI. In this article, we focus on the nonblind HSI deblurring and show that the additional spectral correlation and nonlocal information would significantly improve the HSI deblurring performance.

HSI Super-Resolution: HSI super-resolution refers to the fusion of an HSI (low spatial but high spectral resolution) with a panchromatic/multispectral image (high spatial but low spectral resolution, usually RGB image). The most popular sparsity promoting methods mainly include the sparse representation [6], [7], [57]–[60] and the matrix factorization approach [5], [61]–[64]. Wei *et al.* [6] applied the dictionary learning embedded in the spectral subspace to exploit the sparsity of HSIs. Dong *et al.* [5] proposed a non-negative structured sparse representation (NSSR) approach with the prior knowledge about spatio-spectral sparsity of the HSI. Analog to classical super-resolution [65], a sparse matrix factorization method [62] borrowed the idea that both the LR HSI and HR RGB image share the same coding coefficients. The HR HSI was then reconstructed by multiplying the learned basis from the HR RGB image and sparse coefficients from the LR HSI. Recently, Dian *et al.* [32] proposed a nonlocal sparse Tucker tensor factorization (NLSTF) model for HSI super-resolution. The interested readers can refer to [66].

III. Weighted Low-Rank Tensor Recovery Model

A. Notations and Preliminaries

In this article, we denote tensors by boldface Euler script letters, for example, $\boldsymbol{\mathcal{X}}$. Matrices are represented as boldface capital letters, for example, $\boldsymbol{X}$; vectors are expressed with boldface lowercase letters, for example, $\boldsymbol{x}$; and scalars are denoted by lowercase letters, for example, x. The ith entry of a vector $\boldsymbol{x}$ is denoted by x_i, element (i, j) of a matrix $\boldsymbol{X}$ is denoted by x_{ij}, and element (i, j, k) of a third-order tensor $\boldsymbol{\mathcal{X}}$ is denoted by x_{ijk}.

Fibers are the higher order analog of matrix rows and columns. A fiber of an N-dimensional tensor is a 1-D vector defined by fixing all indices but one [67]. A *Slice* of an N-dimensional tensor is a 2-D matrix defined by fixing all but two indices [67]. For a third-order tensor, its column, row, and tube fibers are denoted by $\boldsymbol{x}_{:jk}, \boldsymbol{x}_{i:k}$, and $\boldsymbol{x}_{ij:}$, respectively.

Definition 1 (Tensor Norms): The *Frobenius* norm of an N-order tensor $\boldsymbol{\mathcal{X}} \in \mathbb{R}^{I_1 \times I_2 \times \cdots \times I_N}$ is the square root of the sum of the squares of all its elements, that is, $||\boldsymbol{\mathcal{X}}||_F = \sqrt{\sum_{i_1=1}^{I_1} \sum_{i_2=1}^{I_2} \cdots \sum_{i_N=1}^{I_N} x_{i_1 i_2 \cdots i_N}^2}$. The $\mathcal{L}_1$ norm of an N-order tensor is the sum of the absolute value of all its elements, that is, $||\boldsymbol{\mathcal{X}}||_1 = \sum_{i_1=1}^{I_1} \sum_{i_2=1}^{I_2} \cdots \sum_{i_N=1}^{I_N} |x_{i_1 i_2 \cdots i_N}|$. These norms for tensor are analogous to the matrix norm.

Definition 2 (Tensor Matricization): Matricization, also called *unfolding or flattening*, is the process of reordering the elements of an N-order tensor into a matrix. The mode-n matricization $\boldsymbol{X}_{(n)} \in \mathbb{R}^{I_n \times (I_1 \cdots I_{n-1} I_n \cdots I_N)}$ of a tensor $\boldsymbol{\mathcal{X}} \in \mathbb{R}^{I_1 \times I_2 \times \cdots \times I_N}$ is obtained by taking all the mode-n fibers to be the columns of the resulting matrix.

Definition 3 (Tensor Product): Here, we just consider the tensor n-mode product, that is, multiplying a tensor by a matrix in mode n, which will be used in HOSVD latter. Interested readers can refer to [67] for a full treatment of tensor multiplication. For a tensor $\boldsymbol{\mathcal{X}} \in \mathbb{R}^{I_1 \times I_2 \times \cdots \times I_N}$, its n-mode product with a matrix $\boldsymbol{U} \in \mathbb{R}^{J \times I_n}$ is denoted by $\boldsymbol{\mathcal{Z}} = \boldsymbol{\mathcal{X}} \times_n \boldsymbol{U}$ and $\boldsymbol{\mathcal{Z}} \in \mathbb{R}^{I_1 \times \cdots \times I_{n-1} \times J \times I_{n+1} \times \cdots \times I_N}$. Each element in $\boldsymbol{\mathcal{Z}}$ can be represented as

$$z_{i_1 \cdots i_{n-1} j i_{n+1} \cdots i_N} = \sum_{i_n=1}^{I_n} x_{i_1 i_2 \cdots i_N} u_{j i_n}. \tag{4}$$

Definition 4 (Tensor SVD): The Tucker decomposition is a kind of HOSVD which decomposes a tensor into a core tensor multiplied by a matrix along each mode [19]

$$\boldsymbol{\mathcal{X}} = \boldsymbol{\mathcal{S}} \times_1 \boldsymbol{U}_1 \times_2 \boldsymbol{U}_2 \times_3 \cdots \times_N \boldsymbol{U}_N \tag{5}$$

where $\boldsymbol{\mathcal{X}} \in \mathbb{R}^{I_1 \times I_2 \times \cdots \times I_N}$, $\boldsymbol{\mathcal{S}} \in \mathbb{R}^{I_1 \times I_2 \times \cdots \times I_N}$ is the *core tensor* similar to the singular values in matrix, and its intensity shows the level of interaction between different components, $\boldsymbol{U}_i \in \mathbb{R}^{I_i \times I_i}$ is the columnwise orthonormal factor matrix and can be regarded as the principal components in each mode. The main purpose of this article is to estimate the core tensors $\boldsymbol{\mathcal{S}}$ and the clean image tensor $\boldsymbol{\mathcal{X}}$ in the presence of the degraded tensor $\boldsymbol{\mathcal{Y}}$, as shown in Fig. 1.

Authorized licensed use limited to: XIDIAN UNIVERSITY. Downloaded on August 13,2026 at 11:06:50 UTC from IEEE Xplore. Restrictions apply.

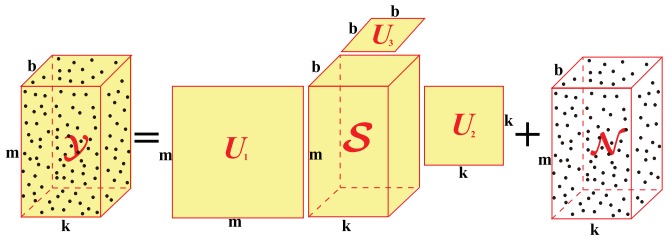


Fig. 1. Illustration of the HOSVD.

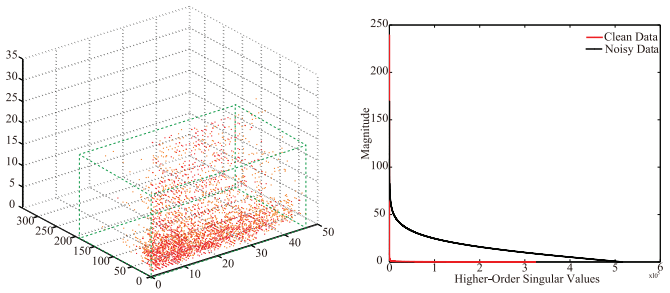


Fig. 2. HOSVD analysis on third-order tensor. (a) Singular values of core tensor bigger than 1. (b) Plot of the singular values of both clean and noisy tensors.

B. WLRTR for 3-D HSI Restoration

1) Why Low-Rank Tensor Recovery: One major shortcoming of 2-D low rank is that it can only work in the presence of two-way (matrix) data. However, the real data, such as HSIs and color images, are ubiquitously in a 3-D way, also referred to as the third-order tensor. To preserve the structural information, we introduce the low-rank tensor recovery model to handle the tensor data by taking advantage of its multidimensional structure.

We apply the HOSVD on the tensor to see how the sparsity of its higher order singular value distributes in a third-order tensor, namely, its higher order low-rank property. In Fig. 2, we give a visualization for facilitating the understanding of the sparsity in the core tensor. There are two observations we make here. First, Fig. 2(a) shows the location of singular values in the core tensor according to their magnitudes. In Fig. 2(a), we can observe that singular values of the core tensor exhibit significant sparsity with different degrees along each mode. More specifically, the magnitude of the singular value shows a general descending tendency along the 2-mode and 3-mode. Along the 2-mode, due to the strong redundancy of the nonlocal cubics, the coefficients in the core tensor along this mode tend to be decreasing very fast to zero. Along the 3-mode, due to the high spectral correlation, the coefficients in the core tensor along this mode tend to decrease to zero at relatively slow speed. Second, from Fig. 2(b), we can observe that singular values of the clean cubic exist much more sparsity than those of the noisy cubics and follow an extremely sharp exponential decay rule. Moreover, the intrinsic sparsity of the higher-order singular values of the 3-D cubic is much more apparent than that of the singular values of the 2-D patch [27]. Therefore, it is natural to use the tensor low-rank model for HSIs recovery problems.

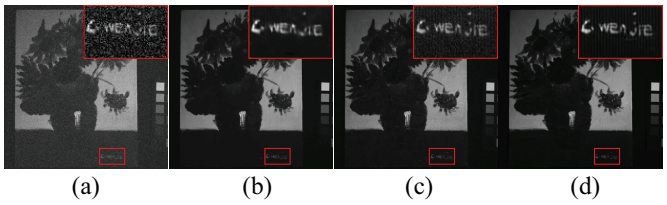


Fig. 3. Advantage of the low-rank tensor recovery over LRMR. (a) Simulated noisy image under Gaussian noise (sigma = 10, PSNR = 28.13 dB). (b) 2-D LRMR result via spatial nonlocal similarity (PSNR = 37.56 dB). (c) 2-D LRMR result via spectral correlation (PSNR = 39.18 dB). (d) 3-D low-rank tensor recovery result (PSNR = 42.95 dB).

In Fig. 3, we give a visual comparison between the third-order cubic recovery and 2-order matrix recovery. Fig. 3(b) shows the result of a 2-D spatial low-rank recovery result, where the low-rank matrix is formed via spatial nonlocal similar patches. Fig. 3(c) shows the result of the 2-D spectral low-rank recovery result, where the low-rank matrix is formed via spectral similar bands. Fig. 3(d) shows the result of the proposed low-rank tensor recovery. It can be inferred from the visual appearance and peak signal-to-noise ratio (PSNR) values that the proposed low-rank tensor recovery method has an obvious advantage over LRMR methods in terms of both noise reduction and texture preserving.

2) Weighted Low-Rank Tensor Recovery Model: For the problem (3), the variable splitting technique [68] is usually introduced to decouple the data fidelity term and regularization term by introducing an auxiliary variable $\mathcal{L}_i$. Consequently, for the regularization-related subproblem, it can be regarded as an image denoising problem as follows:

$$\Phi(\mathcal{L}_i) = \sum_i \frac{1}{\sigma_i^2}\|\mathcal{R}_i\mathcal{X} - \mathcal{L}_i\|_F^2 + \text{rank}(\mathcal{L}_i) \tag{6}$$

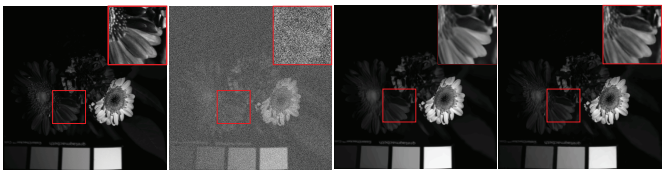
where $\mathcal{R}_i\mathcal{X}$ is the constructed third-order tensor for each exemplar cubic at location i, and our goal is to estimate the corresponding low-rank approximation $\mathcal{L}_i$ under noise variance σ_i^2.

The low-rank regularization has been widely used in matrix recovery and the nuclear norm is usually introduced as the surrogate functional of low-rank constraint. In this article, we borrow this notion in a 2-D matrix to define the tensor nuclear norm of $\mathcal{L}_i$ as $||\mathcal{L}_i||_* = \sum_j |\sigma_j(\mathcal{L}_i)|_1$, namely, the sum of its higher order singular values. Then, the low-rank tensor $\mathcal{L}_i$ can be recovered by solving the following optimization problem:

$$\hat{\mathcal{L}}_i = \arg\min_{\mathcal{L}_i} \frac{1}{\sigma_i^2}\|\mathcal{R}_i\mathcal{X} - \mathcal{L}_i\|_F^2 + \|\mathcal{L}_i\|_*. \tag{7}$$

However, this tensor nuclear norm has not considered the fine-grained sparsity configurations inside the coefficient tensor. As seen in Fig. 2(b), the singular values of clean tensor $\mathcal{R}_i\mathcal{X}$ exhibit strong sparsity in which most of the singular values are close to zero. For the singular values of its corresponding noisy tensor, the larger singular values are close to the singular values of the clean tensor, while the small and trivial singular values are obviously larger than the singular values of the clean tensor. This phenomenon motivates us to penalize the larger singular values less and small singular values more.

Authorized licensed use limited to: XIDIAN UNIVERSITY. Downloaded on August 13,2026 at 11:06:50 UTC from IEEE Xplore. Restrictions apply.



(a) (b) (c) (d)

Fig. 4. Effectiveness of the adaptive weighted strategy. (a) Original clean image. (b) Simulated noisy image band 15 under Gaussian noise (sigma = 30, PSNR = 18.59 dB). (c) Denoising result of the proposed method without adaptive weighted strategy (PSNR = 41.27 dB). (d) Denoising result of the proposed method (PSNR = 41.85 dB).

Thus, we replace the conventional tensor nuclear norm with the weighted one on $\mathcal{L}_i$

$$\hat{\mathcal{L}}_i = \arg\min_{\mathcal{L}_i} \frac{1}{\sigma_i^2}\|\mathcal{R}_i\mathcal{X} - \mathcal{L}_i\|_F^2 + \|\mathcal{L}_i\|_{\boldsymbol{w},*} \tag{8}$$

where $\|\mathcal{L}_i\|_{\boldsymbol{w},*} = \sum_j |w_j\sigma_j(\mathcal{L}_i)|_1$, $\boldsymbol{w} = [w_1, \ldots, w_n]$, and w_j is a non-negative weight assigned to $\sigma_j(\mathcal{L}_i)$. The intuitions behind this weighted process is two-fold. On the one hand, larger singular values corresponding to the major projection orientations should be penalized less to preserve the major data components. On the other hand, the success of the reweighting strategy, where the regularization parameter is adaptive and inversely proportional to the underlying signal magnitude, has been verified in the various computer vision task [34], [69]. For a small value after t iteration, due to the reweighted process in sparsity constraint, it will enforce a larger reweighting factor in the next $t+1$ iteration, which would naturally result in a sparser result. In this article, we set

$$w_j^{t+1} = c \Big/ \left(\left|\sigma_j^t(\mathcal{L}_i)\right| + \varepsilon\right) \tag{9}$$

where $c = 0.04$ is a constant and ε is a small constant to avoid dividing by zero. In Fig. 4, we give a visual comparison between the LRTR model with/without the weighted strategy. The result of Fig. 4(d) exhibits sharper edges than that of without reweighted strategy, which demonstrates the effectiveness of the sparsity reweight strategy in higher order singular values.

3) Optimization of (8): By replacing $\mathcal{L}_i$ in (8) with the corresponding HOSVD, we obtain the following problem:

$$\begin{aligned}\left\{\hat{\mathcal{S}}_i, \hat{\boldsymbol{U}}_1, \hat{\boldsymbol{U}}_2, \hat{\boldsymbol{U}}_3\right\} = & \arg\min_{\mathcal{S}_i, \boldsymbol{U}_1, \boldsymbol{U}_2, \boldsymbol{U}_3} \\ & \times \|\mathcal{R}_i\mathcal{X} - \mathcal{S}_i\times_1\boldsymbol{U}_1\times_2\boldsymbol{U}_2\times_3\boldsymbol{U}_3\|_F^2 \\ & + \sigma_i^2\|\boldsymbol{w}_i \circ \mathcal{S}_i\|_1 \\ & \text{s.t. } \boldsymbol{U}_j{}^T\boldsymbol{U}_j = \boldsymbol{I},\ j = 1, 2, 3\end{aligned} \tag{10}$$

where $\circ$ denotes the elementwise multiplication and j means the mode index of a third-order tensor. There are four variables $\boldsymbol{U}_1$, $\boldsymbol{U}_2$, and $\boldsymbol{U}_3$ along with $\mathcal{S}_i$ to be estimated iteratively.

Update Singular Matrix $\boldsymbol{U}_j$: Since the optimization of $\boldsymbol{U}_1$, $\boldsymbol{U}_2$, and $\boldsymbol{U}_3$ is similar, we take $\boldsymbol{U}_1$ as an example. Dropping out the irrelevant variables from $\boldsymbol{U}_1$ in (10), we can obtain the following subproblem:

$$\hat{\boldsymbol{U}}_1 = \arg\min_{\boldsymbol{U}_1{}^T\boldsymbol{U}_1 = \boldsymbol{I}} \|\mathcal{A}_i - \mathcal{S}_i\times_1\boldsymbol{U}_1\times_2\boldsymbol{U}_2\times_3\boldsymbol{U}_3\|_F^2 \tag{11}$$

where $\mathcal{A}_i = \mathcal{R}_i\mathcal{X} \in \mathbb{R}^{I_1\times I_2\times I_3}$ for simplicity. Xie *et al.* [25] have provided a solution to optimize $\boldsymbol{U}_1$, $\boldsymbol{U}_2$, and $\boldsymbol{U}_3$ via the *von Neumann's trace inequality for the matrix* [70]. Interested readers could refer to [25]. The details can also be found in the supplementary material.

Update Core Tensor $\mathcal{S}_i$: By ignoring terms independent of core tensor $\mathcal{S}_i$ in (10), we obtain the following subproblem:

$$\begin{aligned}\hat{\mathcal{S}}_i = & \arg\min_{\mathcal{S}_i}\|\mathcal{R}_i\mathcal{X} - \mathcal{S}_i\times_1\boldsymbol{U}_1\times_2\boldsymbol{U}_2\times_3\boldsymbol{U}_3\|_F^2 \\ & + \sigma_i^2\|\boldsymbol{w}_i \circ \mathcal{S}_i\|_1.\end{aligned} \tag{12}$$

We follow the technique in [25], where $\|\mathcal{S}_i \times \boldsymbol{U}\|_F^2 = \|\mathcal{S}_i\|_F^2\ \forall \boldsymbol{U}^T\boldsymbol{U} = \boldsymbol{I}$. That is to say, the product of a tensor by the columns orthogonal matrix does not change the strength of the signal. Therefore, we can obtain

$$\hat{\mathcal{S}}_i = \arg\min_{\mathcal{S}_i}\|\mathcal{S}_i - \mathcal{O}_i\|_F^2 + \sigma_i^2\|\boldsymbol{w}_i \circ \mathcal{S}_i\|_1 \tag{13}$$

where $\mathcal{O}_i = (\mathcal{R}_i\mathcal{X})\times_1\boldsymbol{U}_1^T\times_2\boldsymbol{U}_2^T\times_3\boldsymbol{U}_3^T$ is for simplicity. Assume that each coefficient in the core tensor as s_{ijk} and o_{ijk}, respectively, the problem (13) can be converted into the scalar format. Since the singular value in the HOSVD could be either negative or positive, we first consider the situation that $s_{ijk} \geq 0$

$$\begin{aligned}&\min_{s_{ijk}} \left(s_{ijk} - o_{ijk}\right)^2 + \sigma_i^2\left|w_{ijk}s_{ijk}\right| \\ &\Leftrightarrow \min_{s_{ijk}} \left(s_{ijk} - o_{ijk}\right)^2 + \sigma_i^2 w_{ijk}s_{ijk} \\ &\Leftrightarrow \min_{s_{ijk}} \left(s_{ijk} - \left(o_{ijk} - \frac{\sigma_i^2 w_{ijk}}{2}\right)\right)^2.\end{aligned} \tag{14}$$

It is easy to derive its closed-form solution as

$$s_{ijk} = \max\left(o_{ijk} - \sigma_i^2 w_{ijk}/2, 0\right). \tag{15}$$

Furthermore, we incorporate the condition $s_{ijk} < 0$ into consideration, we can obtain the final solution

$$\mathcal{S}_i = \text{sign}(\mathcal{O}_\text{i})\max\left(|\mathcal{O}_\text{i}| - \boldsymbol{w}_\text{i}\sigma_\text{i}^2/2, 0\right). \tag{16}$$

The variables $\boldsymbol{U}_1, \boldsymbol{U}_2, \boldsymbol{U}_3$, and $\mathcal{S}_i$ have been updated alternately with closed-form solutions. The main procedure of the alternating minimization of each variable is similar to [25]. It is worth noting that (8) is very similar to that of the 2-D WNNM [71], which employs the *von Neuman's trace inequality for matrix* [70] to solve the problem. However, *von Neuman's trace inequality for tensor* [72] cannot be directly applied to solve (8). The *von Neuman's trace inequality holds for tensor* with two additional conditions: 1) the diagonal condition and 2) the proportional condition. Interested readers could refer to [72] for details. The diagonal condition is satisfied from both theoretical viewpoint (Tucker decomposition can be regarded as a special case of block-term decomposition (BTD) [73]) and experimental viewpoint (Fig. 2). As for the proportional condition, such a strong assumption cannot be easily satisfied in HSI. The exploration toward the unified optimization for both the 2-D and higher order WNNM would be an interesting topic.

Authorized licensed use limited to: XIDIAN UNIVERSITY. Downloaded on August 13,2026 at 11:06:50 UTC from IEEE Xplore. Restrictions apply.

IV. HSI Restoration With the WLRTR Model

A. WLRTR for HSI Denoising

For HSI denoising, we only consider the random noise $\mathcal{N}$ with an identity tensor operator. Thus, by combining the data fidelity term $\frac{1}{2}||\mathcal{Y}-\mathcal{X}||_F^2$ with the WLRTR prior, (3) can be formulated as the following minimization problem:

$$\left\{\hat{\mathcal{X}},\hat{\mathcal{S}}_i,\hat{U}_j\right\}=\arg\min_{\mathcal{X},\mathcal{S}_i,U_j}\frac{1}{2}\|\mathcal{Y}-\mathcal{X}\|_F^2+\eta\sum_i\Big(\|\mathcal{R}_i\mathcal{X}-\mathcal{S}_i\times_1U_1\times_2U_2\times_3U_3\|_F^2+\sigma_i^2\|\boldsymbol{w}_i\circ\mathcal{S}_i\|_1\Big). \quad (17)$$

The alternating minimization strategy is introduced to solve (17). The closed-form solutions of $\mathcal{S}_i$ and U_j related subproblems (10) have been analyzed. Thus, we can reconstruct the entire image $\mathcal{X}$ by solving the following subproblem:

$$\hat{\mathcal{X}}=\arg\min_{\mathcal{X}}\frac{1}{2}\|\mathcal{Y}-\mathcal{X}\|_F^2+\eta\sum_i\|\mathcal{R}_i\mathcal{X}-\mathcal{S}_i\times_1U_1\times_2U_2\times_3U_3\|_F^2. \quad (18)$$

Equation (18) is a quadratic optimization problem admitting a closed-form solution

$$\mathcal{X}=\left(I+\eta\sum_i\mathcal{R}_i^T\mathcal{R}_i\right)^{-1}\times\left(\mathcal{Y}+\eta\sum_i\left(\mathcal{R}_i^T\mathcal{S}_i\right)\times_1U_1\times_2U_2\times_3U_3\right) \quad (19)$$

where $\eta\sum_i\mathcal{R}_i^T\mathcal{R}_i$ denotes the number of overlapping cubics that cover the pixel location, and $\eta\sum_i(\mathcal{R}_i^T\mathcal{S}_i)\times_1U_1\times_2U_2\times_3U_3$ means the sum value of all overlapping reconstruction cubics that cover the pixel location. Equation (19) can be computed in a tensor format efficiently.

After obtaining an improved estimate of the unknown image, the low-rank tensor approximation (LRTA) can be updated by (10). The updated $\mathcal{S}_i$ and U_j are fed back to (19) improving the estimate of $\mathcal{X}$. Such a process is iterated until the convergence. The overall procedure is summarized in Algorithm 1.

B. WLRTR-RPCA for HSI Destriping

In real HSI, there always exists system structural noise such as stripe noise. The stripes in HSIs via push-broom imaging spectrometer are always nonperiodic and arise from the unstable detectors during a scanning cycle. Therefore, it is natural for us to borrow the RPCA model [9] to accommodate the sparse error component, mainly the stripe noise $\mathcal{E}$. The RPCA has shown its robustness in the presence of the sparse error, such as background subtraction [71], structure noise removal [17], and face recognition under occlusion [74], since it has taken the sparse error into consideration.

In this section, we extend the WLRTR to the WLRTR-RPCA for stripe noise removal. For the image prior, we will utilize the weighted low-rank tensor prior to model them. While for the stripe noise with obviously directional characteristic, as shown in Fig. 5, we argue the $L_{2,1}$-norm with direction discriminative ability is more appropriate than L_1-norm. Since $L_{2,1}$-norm $||\boldsymbol{E}||_{2,1}=\sum_{j=1}^{C}\sqrt{\sum_{i=1}^{R}(E_{ij})^2}$ encourages the intensity of columns to be zero, the underlying assumption here is that the corruptions are sample specific, that is, some data vectors are corrupted and the others are clean, just corresponding to the broken and intact detectors, respectively.

In this article, we extend the matrix $L_{2,1}$-norm to its third-order tensor case $||\mathcal{E}||_{2,1,1}=\sum_{k=1}^{B}\sum_{j=1}^{C}\sqrt{\sum_{i=1}^{R}(E_{ijk})^2}$, and incorporate it into the WLRTR model as follows:

$$\left\{\hat{\mathcal{X}},\hat{\mathcal{E}},\hat{\mathcal{S}}_i,\hat{U}_j\right\}=\arg\min_{\mathcal{X},\mathcal{E},\mathcal{S}_i,U_j}\frac{1}{2}\|\mathcal{Y}-\mathcal{X}-\mathcal{E}\|_F^2+\rho\|\mathcal{E}\|_{2,1,1}+\eta\sum_i\Big(\|\mathcal{R}_i\mathcal{X}-\mathcal{S}_i\times_1U_1\times_2U_2\times_3U_3\|_F^2+\sigma_i^2\|\boldsymbol{w}_i\circ\mathcal{S}_i\|_1\Big) \quad (20)$$

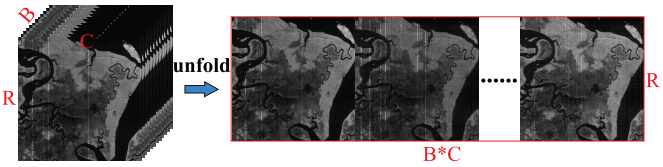
where ρ and η are the regularization parameters. The WLRTR-RPCA model (20) is simple and easy to understand, in which the local sparsity, nonlocal similarity, and spectral consistency of the images are utilized via the tensor low-rank prior, whereas the stripe noise is well depicted by the $L_{2,1}$-norm, so that the mixed random and stripe noise can be separated from the images satisfactorily.

The procedures of estimation $\mathcal{S}_i$ and $\mathcal{X}$ are similar with Algorithm 1. Here, we show how we estimate $\mathcal{E}$. Once $\mathcal{S}_i$ and $\mathcal{X}$ have been estimated, we can estimate $\mathcal{E}$ by solving the following subproblem:

$$\hat{\mathcal{E}}=\arg\min_{\mathcal{E}}\frac{1}{2}\|\mathcal{Y}-\mathcal{X}-\mathcal{E}\|_F^2+\rho\|\mathcal{E}\|_{2,1,1}. \quad (21)$$

Algorithm 1 WLRTR for HSI Denoising

Require: Noisy image $\mathcal{Y}$
1: **procedure** DENOISING
2: **Initialize:** Set parameters η; $\mathcal{X}^{(1)}=\mathcal{Y}$;
3: **for** n=1:N **do**
4: Step1: Similar cubics grouping: low-rank Tensor;
5: **for** (Low-rank tensor approximation) i=1:I **do**
6: Step2: Update the weight using Eq. (9);
7: Step3: Solve Eq. (11) for the singular matrix U_j;
8: Step4: Estimate the core tensor $\mathcal{S}_i$ via Eq. (16);
9: **end for**
10: Step5: Reconstruct the whole image $\mathcal{X}$ via Eq.(19).
11: **end for**
Ensure: Clean image $\mathcal{X}$



(a) (b)

Fig. 5. Illustration of HSI stripe mode-1 unfolding. (a) Original HSI cubic with vertical stripe. (b) Mode-1 unfolding matrix.

Authorized licensed use limited to: XIDIAN UNIVERSITY. Downloaded on August 13,2026 at 11:06:50 UTC from IEEE Xplore. Restrictions apply.

Algorithm 2 WLRTR-RPCA for HSI Destriping

Require: Noisy image $\mathcal{Y}$
procedure DESTRIPING
  Initialize: Set parameters η and ρ; $\mathcal{X}^{(1)} = \mathcal{Y}$;
  for n=1:N **do**
    Step 1: Update sparse error $\mathcal{E}$ by solving (21);
    Step 2: Update clean image $\mathcal{X}$ by **Algorithm 1**.
  end for
Ensure: Clean image $\mathcal{X}$ and stripe component $\mathcal{E}$.

It is hard to directly obtain the final result. However, we have the following Lemma [75]: Let $\boldsymbol{Q} = [\boldsymbol{q}_1, \boldsymbol{q}_2, \ldots, \boldsymbol{q}_i, \ldots]$ be a given matrix and $\| \bullet \|_F$ be the Frobenius norm. If $\hat{\boldsymbol{W}}$ is the optimal solution of

$$\hat{\boldsymbol{W}} = \arg\min_{\boldsymbol{W}} \frac{1}{2}\|\boldsymbol{W} - \boldsymbol{Q}\|_F^2 + \mu\|\boldsymbol{W}\|_{2,1}$$

then the ith column of $\hat{\boldsymbol{W}}$ is

$$\hat{\boldsymbol{W}}(:, i) = \begin{cases} \frac{\|\boldsymbol{q}_i\| - \mu}{\|\boldsymbol{q}_i\|}\boldsymbol{q}_i, & \text{if } \mu \le \|\boldsymbol{q}_i\| \\ 0, & \text{otherwise.} \end{cases}$$

Thus, it is natural for us to unfold the tensors into the matrix (tensor matricization) so that we can apply lemma directly. By unfolding of the tensors along mode-1, (21) is converted into the equivalent problem

$$\hat{\boldsymbol{E}}_{(1)} = \arg\min_{\boldsymbol{E}_{(1)}} \|\boldsymbol{Y}_{(1)} - \boldsymbol{X}_{(1)} - \boldsymbol{E}_{(1)}\|_F^2 + \rho\|\boldsymbol{E}_{(1)}\|_{2,1}. \quad (22)$$

Equation (22) can be solved efficiently via lemma. It is worth noting that we chose the mode-1 unfolding since only in this way the resulting matrix still preserves the directional characteristic [Fig. 5(b)], while mode-2 and mode-3 unfolding may lose this property. After we obtain the sparse error matrix $\hat{\boldsymbol{E}}_{(1)}$, we fold it into the tensor format. The overall procedure is summarized in Algorithm 2.

C. WLRTR for HSI Deblurring

For HSI deblurring, we only consider the random noise $\mathcal{N}$ with the blurring operator. Thus, by combining the data fidelity term $(1/2)\|\mathcal{Y} - \mathcal{T}(\mathcal{X})\|_F^2$ with the WLRTR prior, (3) can be formulated as the following minimization problem:

$$\begin{aligned}\left\{\hat{\mathcal{X}}, \hat{\mathcal{S}}_i, \hat{\boldsymbol{U}}_j\right\} = \arg\min_{\mathcal{X}, \mathcal{S}_i, \boldsymbol{U}_j} &\frac{1}{2}\|\mathcal{Y} - \mathcal{X} * \mathcal{H}\|_F^2 \\ &+ \eta\sum_i \Big(\|\mathcal{R}_i\mathcal{X} - \mathcal{S}_i \times_1 \boldsymbol{U}_1 \times_2 \boldsymbol{U}_2 \times_3 \boldsymbol{U}_3\|_F^2 \\ &+ \sigma_i^2\|\boldsymbol{w}_i \circ \mathcal{S}_i\|_1\Big) \end{aligned} \quad (23)$$

where $*$ denotes the convolution operator and $\mathcal{H}$ is a linear shift-invariant point spread function (PSF). Here, we do not take the stripe noise component $\mathcal{E}$ into consideration. Joint destriping and deblurring for HSI is another much harder problem, which is out of the scope of this article. For the problem (23), we employ the alternating direction method of multipliers (ADMM) [68] by introducing auxiliary variable $\mathcal{B} = \mathcal{X}$ to decouple the fidelity from regularization term

$$\hat{\mathcal{B}} = \arg\min_{\mathcal{B}} \frac{1}{2}\|\mathcal{Y} - \mathcal{B} * \mathcal{H}\|_F^2 + \frac{\alpha}{2}\left\|\mathcal{B} - \mathcal{X} - \frac{\mathcal{J}}{\alpha}\right\|_F^2 \quad (24a)$$

Algorithm 3 WLRTR for HSI Deblurring

Require: Blurring image $\mathcal{Y}$ and PSF $\mathcal{H}$
procedure DEBLURRING
  Initialize: Set parameters η, α, δ; $\mathcal{X}^{(1)} = \mathcal{Y}$;
  for n=1:N **do**
    Step 1: Image deconvolution $\mathcal{B}$ by solving (24a);
    Step 2: Image reconstruction $\mathcal{X}$ by solving (24b);
    for (Low-rank tensor approximation) i=1:I **do**
      Step 3: Update the weight using Eq. (9);
      Step 4: Solve Eq. (24c)) for the singular matrix $\boldsymbol{U}_j$;
      Step 5: Estimate $\mathcal{S}_i$ by solving (24d);
    end for
    Step 6: Lagrangian multipliers update via (27);
  end for
Ensure: Clean image $\mathcal{X}$.

$$\hat{\mathcal{X}} = \arg\min_{\mathcal{X}} \frac{\alpha}{2}\left\|\mathcal{B} - \mathcal{X} - \frac{\mathcal{J}}{\alpha}\right\|_F^2 + \eta\sum_i \|\mathcal{R}_i\mathcal{X} - \mathcal{S}_i \times_1 \boldsymbol{U}_1 \times_2 \boldsymbol{U}_2 \times_3 \boldsymbol{U}_3\|_F^2 \quad (24b)$$

$$\hat{\boldsymbol{U}}_j = \arg\min_{\boldsymbol{U}_j^T\boldsymbol{U}_j = \boldsymbol{I}} \|\mathcal{R}_i\mathcal{X} - \mathcal{S}_i \times_1 \boldsymbol{U}_1 \times_2 \boldsymbol{U}_2 \times_3 \boldsymbol{U}_3\|_F^2 \quad (24c)$$

$$\hat{\mathcal{S}}_i = \arg\min_{\mathcal{S}_i} \|\mathcal{R}_i\mathcal{X} - \mathcal{S}_i \times_1 \boldsymbol{U}_1 \times_2 \boldsymbol{U}_2 \times_3 \boldsymbol{U}_3\|_F^2 + \sigma_i^2\|\boldsymbol{w}_i \circ \mathcal{S}_i\|_1 \quad (24d)$$

where $\mathcal{J}$ is the corresponding Lagrangian multiplier and α is a positive scalar. Equation (24a) performs the image deconvolution, (24b) means the image denoising process, and (24c) and (24d) denote the LRTA.

According to Plancherel's theorem [76], the sum of the square of a function equals the sum of the square of its Fourier transform. In view of the convolution operator in (24a), we operate in the frequency domain using 3-D fast Fourier transforms (3-D FFT) to make the computation efficient. Thus, we can transform (24a) into the following:

$$\begin{aligned}\mathcal{F}(\hat{\mathcal{B}}) = \arg\min_{\mathcal{F}(\mathcal{B})} &\frac{1}{2}\|\mathcal{F}(\mathcal{Y}) - \mathcal{F}(\mathcal{B}) \circ \mathcal{F}(\mathcal{H})\|_F^2 \\ &+ \frac{\alpha}{2}\left\|\mathcal{F}(\mathcal{B}) - \mathcal{F}(\mathcal{X}) - \mathcal{F}\left(\frac{\mathcal{J}}{\alpha}\right)\right\|_F^2. \end{aligned} \quad (25)$$

The closed-form solution of (25) can be expressed as

$$\hat{\mathcal{B}} = \mathcal{F}^{-1}\left(\frac{\mathcal{F}^*(\mathcal{H}) \circ \mathcal{F}(\mathcal{Y}) + \alpha\mathcal{F}(\mathcal{X}) + \mathcal{F}(\mathcal{J})}{\mathcal{F}^*(\mathcal{H}) \circ \mathcal{F}(\mathcal{H}) + \alpha\mathcal{I}}\right) \quad (26)$$

where $\mathcal{F}$, $\mathcal{F}^*$, and $\mathcal{F}^{-1}$ denote the FFT operator, its conjugate, and its inverse, respectively. The solution of $\mathcal{X}$ in (24b) can be calculated similar to that of (18), and the LRTA $\mathcal{S}_i$ and $\boldsymbol{U}_j$ can be updated by solving (10). Finally, the Lagrangian multipliers and penalization parameter are updated as follows:

$$\begin{cases} \mathcal{J}^{k+1} = \mathcal{J}^k + \alpha\left(\mathcal{X} - \mathcal{B}^{k+1}\right) \\ \alpha^{k+1} = \delta \cdot \alpha^k. \end{cases} \quad (27)$$

The overall procedure is summarized in Algorithm 3.

D. WLRTR for HSI Super-Resolution

For HSI super-resolution, we consider the random noise $\mathcal{N}$ with both the blurring and downsampling in spatial domain

Authorized licensed use limited to: XIDIAN UNIVERSITY. Downloaded on August 13,2026 at 11:06:50 UTC from IEEE Xplore. Restrictions apply.

$\mathcal{Y}$, as well as downsampling in spectral domain $\mathcal{Z}$. Thus, (3) can be formulated as the following minimization problem:

$$\left\{\hat{\mathcal{X}}, \hat{\mathcal{S}}_i, \hat{U}_j\right\} = \arg\min_{\mathcal{X},\mathcal{S}_i,U_j} \frac{1}{2}\|\mathcal{Y}-\mathcal{T}_{sa}(\mathcal{X})\|_F^2+\frac{1}{2}\|\mathcal{Z}-\mathcal{T}_{se}(\mathcal{X})\|_F^2 + \eta\sum_i\Big(\|\mathcal{R}_i\mathcal{X}-\mathcal{S}_i\times_1 U_1\times_2 U_2\times_3 U_3\|_F^2 + \sigma_i^2\|w_i\circ\mathcal{S}_i\|_1\Big). \tag{28}$$

Since the variable splitting methods could separate each term with physical meanings, for the problem HSI super-resolution with both spatial and spectral degradations, we also employ the ADMM [68] by introducing two auxiliary variables $\mathcal{Q}=\mathcal{X}$ and $\mathcal{G}=\mathcal{X}$ to decouple the two data fidelity terms from the regularization term as follows:

$$\hat{\mathcal{Q}} = \arg\min_{\mathcal{Q}} \frac{1}{2}\|\mathcal{Y}-\mathcal{T}_{sa}(\mathcal{Q})\|_F^2+\frac{\beta}{2}\left\|\mathcal{Q}-\mathcal{X}-\frac{\mathcal{J}_1}{\beta}\right\|_F^2 \tag{29a}$$

$$\hat{\mathcal{G}} = \arg\min_{\mathcal{G}} \frac{1}{2}\|\mathcal{Z}-\mathcal{T}_{se}(\mathcal{G})\|_F^2+\frac{\gamma}{2}\left\|\mathcal{G}-\mathcal{X}-\frac{\mathcal{J}_2}{\gamma}\right\|_F^2 \tag{29b}$$

$$\hat{\mathcal{X}} = \arg\min_{\mathcal{X}} \eta\sum_i\|\mathcal{R}_i\mathcal{X}-\mathcal{S}_i\times_1 U_1\times_2 U_2\times_3 U_3\|_F^2 + \frac{\beta}{2}\left\|\mathcal{Q}-\mathcal{X}-\frac{\mathcal{J}_1}{\beta}\right\|_F^2+\frac{\gamma}{2}\left\|\mathcal{G}-\mathcal{X}-\frac{\mathcal{J}_2}{\gamma}\right\|_F^2 \tag{29c}$$

$$\hat{U}_j = \arg\min_{U_j^T U_j=I}\|\mathcal{R}_i\mathcal{X}-\mathcal{S}_i\times_1 U_1\times_2 U_2\times_3 U_3\|_F^2 \tag{29d}$$

$$\hat{\mathcal{S}}_i = \arg\min_{\mathcal{S}_i}\|\mathcal{R}_i\mathcal{X}-\mathcal{S}_i\times_1 U_1\times_2 U_2\times_3 U_3\|_F^2+\sigma_i^2\|w_i\circ\mathcal{S}_i\|_1 \tag{29e}$$

where $\mathcal{J}_1$ and $\mathcal{J}_2$ are the corresponding Lagrangian multipliers, and α and β are positive scalars. Equations (29a) and (29b) perform the HSI spatial and spectral super-resolution, respectively, (29c) denotes the image reconstruction, and (29d) and (29e) represent the LRTA. Each subproblem has a closed-form solution. For (29a) and (29b), the subproblems can be solved by computing

$$\mathcal{T}_{\text{comp}}(\mathcal{Q}) = \mathcal{T}_{sa}^T(\mathcal{Y})+\beta\mathcal{X}+\mathcal{J}_1 \tag{30}$$

$$\mathcal{G}\times_3\left(P^TP+\gamma I\right) = \mathcal{Z}\times_3 P^T+\gamma\mathcal{X}+\mathcal{J}_2 \tag{31}$$

where $\mathcal{T}_{\text{comp}} = \mathcal{T}_{sa}^T\mathcal{T}_{sa}+\beta\mathcal{I}$ is the composite operator on $\mathcal{Q}$, and $\mathcal{T}_{sa}^T(\mathcal{Y})$ means the transposed blurring and downsampling on $\mathcal{Y}$. Since it is hard for us to calculate (30) and (31) directly, in our implementation, we unfold the 3-D tensors along the mode-3 to the 2-D matrices as [5]. The solution of $\mathcal{X}$ in (29c) can be calculated similar to that of (18) and the low-rank tensors $\hat{\mathcal{S}}_i$ can be updated by (10). Finally, the Lagrangian multipliers and penalization parameter are updated as follows:

$$\begin{cases}\mathcal{J}_1{}^{k+1} = \mathcal{J}_1{}^k+\beta\left(\mathcal{X}-\mathcal{Q}^{k+1}\right)\\ \mathcal{J}_2{}^{k+1} = \mathcal{J}_2{}^k+\gamma\left(\mathcal{X}-\mathcal{G}^{k+1}\right)\\ \beta^{k+1}=\delta\cdot\beta^k,\ \gamma^{k+1}=\delta\cdot\gamma^k.\end{cases} \tag{32}$$

The overall procedure is summarized in Algorithm 4.

Algorithm 4 WLRTR for HSI Super-Resolution

Require: Spatial and spectral LR image $\{\mathcal{Y}, \mathcal{Z}\}$, PSF $\mathcal{H}$
procedure SUPER-RESOLUTION
  Initialize: $\eta, \beta, \gamma, \delta$; $\mathcal{X}^{(1)} = \uparrow_{upsampling}(\mathcal{Y})$;
  for n=1:N **do**
    Step 1: Spatial SR $\mathcal{Q}$ by solving (29a);
    Step 2: Spectral SR $\mathcal{G}$ by solving (29b);
    Step 3: Image reconstruction $\mathcal{X}$ by solving (29c);
    for (Low-rank tensor approximation) i=1:I **do**
      Step 4: Update the weight using Eq. (9);
      Step 5: Solve Eq. (29d)) for the singular matrix U_j;
      Step 6: Estimate $\mathcal{S}_i$ by solving (29e);
    end for
    Step 7: Lagrangian multipliers update via (32);
  end for
Ensure: Clean image $\mathcal{X}$.

V. EXPERIMENTAL RESULTS

A. Experimental Setting

Benchmark Datasets: We test three HSIs datasets.

1) *Columbia Multispectral Database (CAVE)*[1]*:* The entire dataset consisting of 32 noiseless HSIs of size $512\times 512\times 31$ are captured with the wavelengths in the range of 400–700 nm at an interval of 10 nm.
2) *Harvard Hyperspectral Datasets (HHD) [77]:* The entire dataset consisting of 50 noisy HSIs of size $1040\times 1392\times 31$ are captured with the wavelengths in the range of 420–720 nm at an interval of 10 nm.
3) *Remotely Sensed HSIs:* Remotely sensed hyperspectral datasets are also used, that is, *Salinas* and *Cuprite*.

Preprocessing: First, before the restoration process, all the original images were coded to an 8-b scale for display convenience and uniform parameter setting. Second, for the nonlocal similarity cubic matching, we do not directly search from 3-D cubics in the noisy data. Instead, for reducing computational load and matching accuracy, we proposed to average each band of the cubic, which can be regarded as a uniform filtering procedure, so that we can obtain a quite clean 2-D matrix. Note that the nonlocal similarity matching processing is performing on this 2-D matrix, while our restoration is still processing on the entire 3-D cubics.

Baselines: For the HSI denoising methods, we compare with block-matching and 3-D filtering (BM3D) [78], parallel factor analysis (PARAFAC) [21], LRTA [79], LRMR [10], adaptive nonlocal means denoising (ANLM) [80], non-negative matrix factorization (NMF) [81], BM4D [39], TDL [23], intrinsic tensor sparsity regularization (ITSReg) [25], hyper-Laplacian (HL) regularized low-rank tensor (LLRT) [27], non independent identically distributed mixture of Gaussians (NMoG) [15], and TV regularized low-rank tensor decomposition (LRTDTV) [50]; for HSI deblurring, the competing methods include single-image-based HL [82], and HSI deblurring methods fast positive deconvolution (FPD) [55] and spectral–spatial TV (SSTV) [56]; and for HSI super-resolution, we compare with coupled NMF (CNMF) [61], NSSR [5], and NLSTF [32].

[1] http://www.cs.columbia.edu/CAVE/databases/multispectral/

Authorized licensed use limited to: XIDIAN UNIVERSITY. Downloaded on August 13,2026 at 11:06:50 UTC from IEEE Xplore. Restrictions apply.

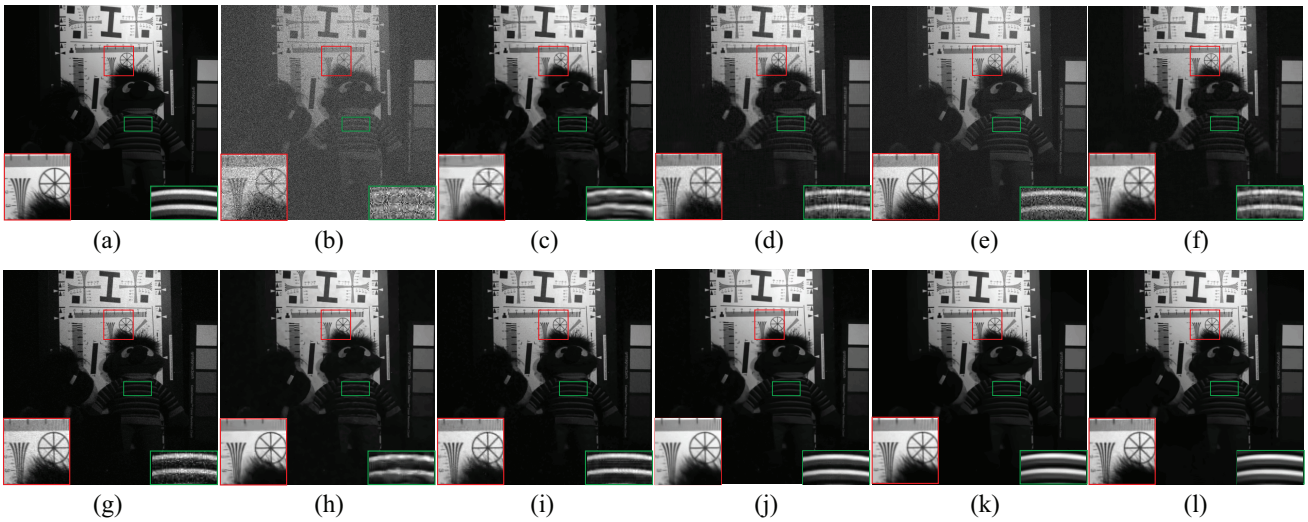


Fig. 6. Simulated random noise removal results under noise level $\sigma^2 = 30$ on the CAVE dataset. (a) Original image *toy* at band 510 nm. (b) Noisy image. Denoising results by (c) BM3D, (d) LRTA, (e) LRMR, (f) LRTDTV, (g) NMF, (h) BM4D, (i) TDL, (j) ITSReg, (k) LLRT, and (l) WLRTR. We show the corresponding quantitative values under the visual results.

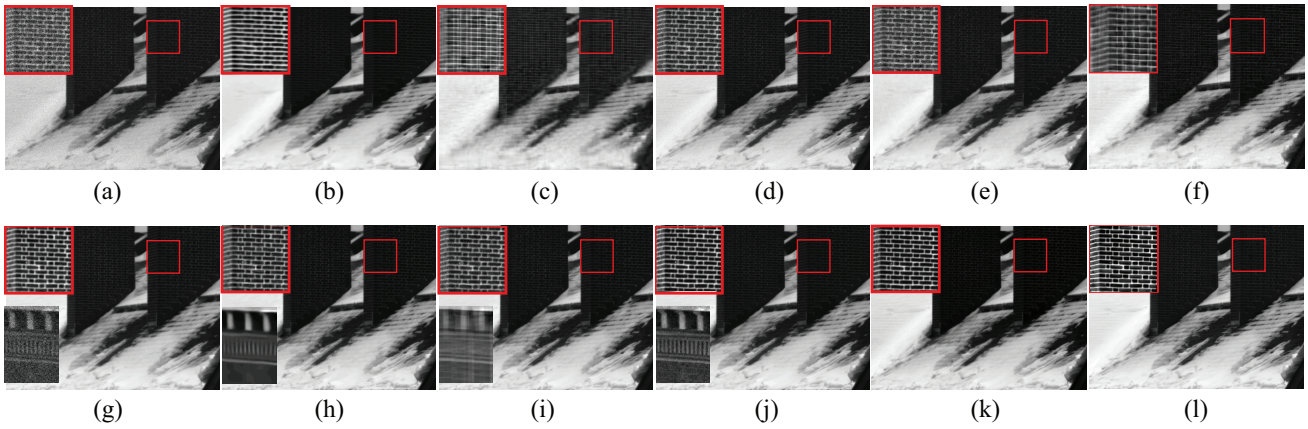


Fig. 7. Real random noise removal results on the HHD dataset. (a) Noisy image. Denoising results by (b) BM3D, (c) PARAFAC, (d) LRTA, (e) ANLM, (f) LRTDTV, (g) NMF, (h) BM4D, (i) TDL, (j) ITSReg, (k) LLRT, and (l) WLRTR.

We use the codes provided by the authors or downloaded them from their homepages and fine-tune the parameters by default or follow the rules in their papers to achieve the best performance. The MATLAB code of our methods can be downloaded from the homepage of the author.[2] For parameter settings of our method, the most important parameter is the number of nonlocal cubics, which is set between [100, 200] in correspondence with the noise level, respectively. The patch size is between [6, 8]. Another important factor is the regularization parameter η for HSI deblurring and super-resolution, which is set as 10^{-8} and 10^{-5}, respectively.

Evaluation Indexes: Four quantitative quality indexes are employed [23], including PSNR, structure similarity (SSIM), erreur relative globale adimensionnelle de synthese (ERGAS), and spectral angle map (SAM). The PSNR and SSIM evaluate the spatial quality, and the ERGAS and SAM assess the spectral quality. The larger PSNR and SSIM values are, the smaller ERGAS and SAM values are, the better the restored images are.

[2]https://owuchangyuo.github.io/

B. HSI Denoising

To visually illustrate the denoising performance of WLRTR, we choose two images *toy* of band 510 nm under noise level $\sigma^2 = 30$, as shown in Fig. 6. In Fig. 6 (the green demarcated window), we can clearly see from the enlarged region that the proposed method has obtained clearer results compared with other competing methods. Moreover, looking at the red demarcated window in Fig. 6, the proposed WLRTR is capable of well reconstructing the tiny hair texture. We also test the proposed WLRTR method on real noisy HSI. Since the noise level is unknown for real noisy images, we adopted an estimation method from [83] to estimate the noise level beforehand. In Fig. 7, from the demarcated window, we can observe that the WLRTR method obtains a smoother image with a clearer texture and line pattern. In summary, WLRTR has obtained better performance in terms of noise suppression, detail preserving, artifacts-free, visual pleasure, and PSNR value under different noise levels.

We also present the overall quantitative assessments of all competing methods on CAVE in Table I. The highest PSNR

Authorized licensed use limited to: XIDIAN UNIVERSITY. Downloaded on August 13,2026 at 11:06:50 UTC from IEEE Xplore. Restrictions apply.

TABLE I
QUANTITATIVE RESULTS OF DIFFERENT METHODS UNDER SEVERAL NOISE LEVELS ON THE CAVE DATASET

σ^2	Index	Methods											
		Noisy	BM3D	PARAFAC	LRTA	LRMR	ANLM	LRTDTV	NMF	BM4D	TDL	ITSReg	LLRT	WLRTR
10	PSNR	28.13	42.09	35.43	41.36	39.27	41.52	40.90	43.15	44.59	44.30	45.77	46.67	**46.85**
	SSIM	0.4371	0.9665	0.8767	0.9499	0.9094	0.9576	0.9510	0.9702	0.9784	0.9797	0.9802	0.9872	**0.9873**
	ERGAS	236.40	45.06	108.37	49.53	64.81	47.78	57.97	39.65	33.33	34.86	30.53	26.74	**25.91**
	SAM	0.7199	0.1395	0.2360	0.1719	0.3343	0.2184	0.1519	0.1358	0.1295	0.1025	0.1086	**0.0841**	0.0863
20	PSNR	22.11	38.46	34.53	38.04	34.38	37.42	39.51	39.02	41.02	41.06	42.54	43.51	**43.67**
	SSIM	0.1816	0.9339	0.8574	0.9119	0.7807	0.8936	0.9380	0.9169	0.9550	0.9638	0.9650	0.9767	**0.9769**
	ERGAS	472.88	68.38	115.81	72.16	113.47	76.15	65.06	63.61	50.38	50.47	44.12	38.82	**37.64**
	SAM	0.9278	0.1984	0.2838	0.2139	0.5009	0.3358	0.1810	0.1946	0.1981	0.1284	0.1171	**0.1042**	0.1067
30	PSNR	18.59	36.40	33.59	36.15	31.36	34.77	37.79	36.53	38.90	39.03	40.51	41.55	**41.68**
	SSIM	0.0988	0.9034	0.8261	0.8787	0.6451	0.8060	0.9115	0.8565	0.9277	0.9486	0.9488	0.9683	**0.9666**
	ERGAS	709.29	88.29	128.07	91.40	157.65	104.95	76.53	86.25	65.38	63.54	53.05	48.20	**47.36**
	SAM	1.0414	0.2489	0.3455	0.2479	0.6021	0.4376	0.2309	0.2465	0.2598	0.1520	0.1374	**0.1192**	0.1248
50	PSNR	14.15	32.66	30.22	32.44	26.67	30.74	34.64	31.98	35.96	36.42	37.75	38.93	**39.06**
	SSIM	0.0432	0.8320	0.7051	0.7932	0.4000	0.6057	0.8226	0.7113	0.8666	0.9175	0.9271	**0.9521**	0.9457
	ERGAS	1181.95	115.06	155.84	118.64	264.28	164.55	106.27	123.23	91.51	85.58	70.16	65.52	**63.83**
	SAM	1.1741	0.2877	0.4460	0.2843	0.7534	0.5806	0.3537	0.3148	0.3575	0.2000	0.1619	**0.1424**	0.1580
100	PSNR	8.13	29.27	26.01	29.20	20.84	24.90	29.19	26.95	30.82	32.91	33.01	**35.40**	35.15
	SSIM	0.0122	0.7460	0.4346	0.6945	0.1850	0.2826	0.5338	0.4643	0.6956	0.8344	0.8648	**0.9143**	0.8876
	ERGAS	2364.05	171.94	253.70	175.91	469.26	324.48	195.38	225.55	141.18	128.22	120.77	**98.91**	100.44
	SAM	1.3271	0.3938	0.6843	0.3381	0.9306	0.7972	0.5986	0.4321	0.5014	0.3079	0.2376	**0.1895**	0.2300

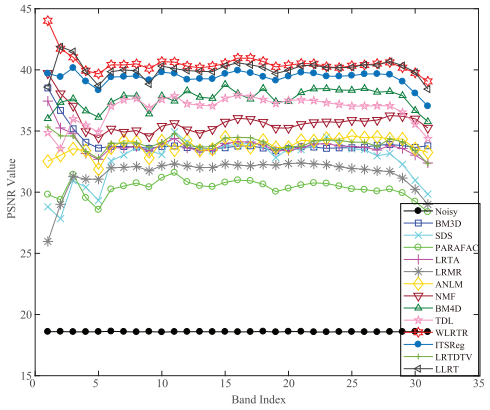


Fig. 8. PSNR values of each band of image *toy* under noise level $\sigma^2 = 30$ on the CAVE dataset.

TABLE II
QUANTITATIVE RESULTS OF THE COMPETING METHODS UNDER DIFFERENT BLUR LEVELS ON THE CAVE DATASET

Methods	HL	FPD	SSTV	DB-WLRTR
Gaussian (8*8, Sigma = 3)				
PSNR	37.28	38.84	37.61	**55.68**
SSIM	0.9460	0.9617	0.9527	**0.9979**
ERGAS	83.88	68.48	80.91	**9.9635**
SAM	0.0676	0.0734	0.0658	**0.0250**
Gaussian (17*17, Sigma = 7)				
PSNR	32.59	33.16	33.08	**49.42**
SSIM	0.8819	0.9114	0.8944	**0.9926**
ERGAS	137.14	125.11	129.84	**20.87**
SAM	0.1075	0.1163	0.0989	**0.0439**

and SSIM values and lowest ERGAS and SAM values are highlighted in bold. We have the following observations. First, WLRTR consistently achieves the best performance in four assessments, which highly demonstrates the effectiveness of WLRTR for HSIs. Second, for random noise in the CAVE, with the increase of noise level, the advantage of our method over other methods becomes more obvious. We can observe that the proposed method almost exceeds 4.3 dB than BM4D at $\sigma^2 = 100$. Furthermore, we plot the PSNR values of each band of one single image *toy* in CAVE as an example, as shown in Fig. 8. It can be observed that the PSNR values of all the bands obtained by WLRTR are significantly higher than those of the other methods.

C. HSI Deblurring

There are relatively fewer researches paying attention to HSI deblurring. We compare the proposed DB-WLRTR method with single-image-based deblurring method HL [82] and two HSI deblurring methods FPD [55] and SSTV [56]. The CAVE dataset is used for the comparison study. The Gaussian blur kernels with different sizes and standard deviations are tested. We assume the PSF is known. From Table II, we can see that the proposed DB-WLRTR has an overwhelming advantage over the other methods under different Gaussian blur levels. The visual comparisons of the deblurring methods are shown in Fig. 9, from which we can see that the DB-WLRTR method produces much cleaner and sharper image edges and textures than other methods. It is noteworthy that the lost details, such as the text and the artificial flower, can be well recovered by our method.

D. HSI Super-Resolution

We also test the proposed SR-WLRTR model on HSI super-resolution. The CAVE dataset is used for the comparison study. Both the Gaussian and uniform blur are tested with scaling factors $s = 8$. We compare the SR-WLRTR with the representative state-of-the-art methods, including both the matrix-based CNMF [61], NSSR [5] and tensor-based NLSTF [32]. The quantitative results are shown in Table III. It can be seen that the results of the proposed method are superior to the competing methods both the spatial and spectral aspects, especially the Gaussian blur. One visual comparison results at

Authorized licensed use limited to: XIDIAN UNIVERSITY. Downloaded on August 13,2026 at 11:06:50 UTC from IEEE Xplore. Restrictions apply.

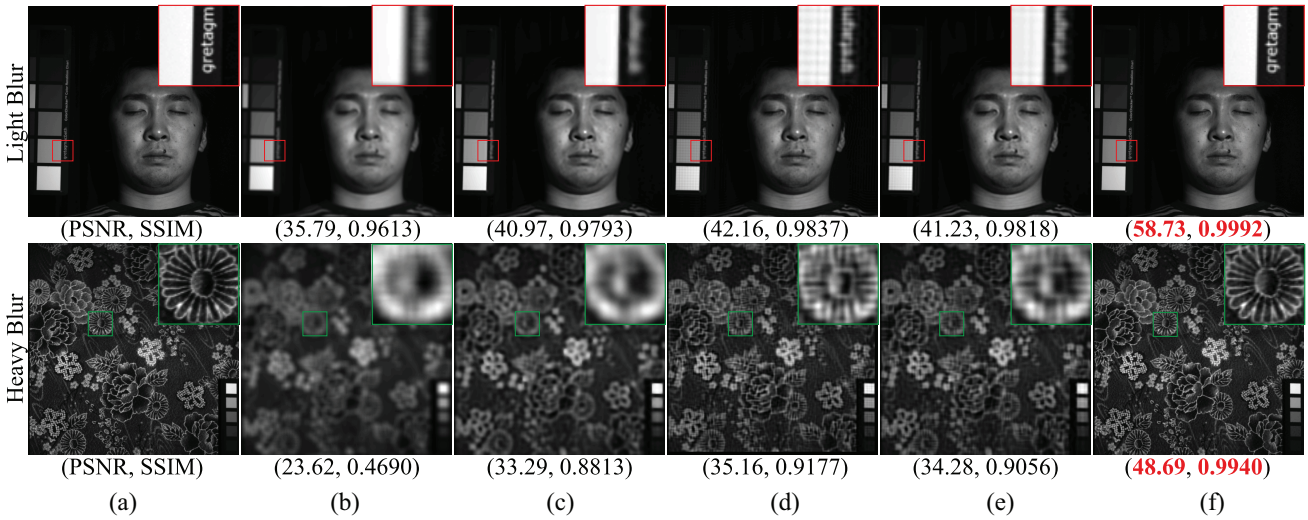


Fig. 9. Simulated deblurring results under different blur levels on the CAVE dataset. The first row shows the light blur case (8*8, sigma = 3) and the second row displays the heavy blur case (17*17, sigma = 7). (a) Original image at band 510 nm. (b) Degraded image. Deblurring results by (c) HL, (d) FPD, (e) SSTV, and (f) DB-WLRTR.

TABLE III
QUANTITATIVE RESULTS OF THE COMPETING METHODS UNDER DIFFERENT DOWNSAMPLING CASES ON THE CAVE DATASET

Methods	CNMF	NLSTF	NSSR	SR-WLRTR
Gaussian (s = 8, 8*8, Sigma = 3)				
PSNR	46.15	44.56	46.99	**47.39**
SSIM	0.9901	0.9816	0.9921	**0.9931**
ERGAS	35.15	41.89	30.21	**29.26**
SAM	0.0591	0.0961	0.0528	**0.0500**
Uniform (s = 8)				
PSNR	46.49	45.00	47.51	**47.57**
SSIM	0.9909	0.9847	0.9931	**0.9934**
ERGAS	34.56	39.06	28.84	**28.82**
SAM	0.0568	0.0869	0.0512	**0.0493**

700 nm of the *flower* by all competing methods are shown in Fig. 10. All the competing methods can well recover the HR spatial structures of the scene, but the proposed method achieves the smallest reconstruction errors, especially for the sharp edges. In conclusion, compared with the matrix-based methods, the SR-WLRTR could better preserve the spatial-spectral structures with better recovering the spatial details and less spectral distortion; compared with the tensor-based methods NLSTF [32], the SR-WLRTR utilizes the low-rank tensor prior in HSI, thus resulting in better visual pleasing result, while there are obvious gridding artifacts in NLSTF.

E. HSI Destriping

In this section, we evaluate the WLRTR-RPCA model on the very common mixed noise in HSIs: random noise and stripe noise. We randomly added the stripe on HSI and the locations of the stripes between the neighbor bands were different. It is worth noting that we do not know the location of the stripes. Fig. 11 displays the noise removal results of the competing methods. It is obvious that there still exist some residual stripes in Fig. 11(c)–(j), which means these methods only work well for the random noise. In Fig. 11(l), the stripes are perfectly removed and the detailed structure information in each image is well preserved without the introduction of any noticeable artifacts. The quantitative mixed noise removal results on both *Salinas* and *Cuprite* datasets are reported in Table IV. It is worth noting that the NMoG obtains a very competitive restoration result with higher quantitative value and better visual appearance. However, we can still observe the residual stripe and random noise in the result of NMoG. Moreover, the performance of NMoG heavily relies on the bands of the input HSI. Overall, the proposed method consistently obtains the best mixed noise removal results both quantitatively and qualitatively.

F. Analysis and Discussion

1) Effectiveness of the Reweight Strategy: Here, we give a comprehensive comparison between the LRTR model with/without the weighted strategy for different tasks, as shown in Table V. We can observe that both the baseline LRTR and WLRTR have significantly improved the restoration results. Moreover, the restoration results of the weighted LRTR are better than those of the LRTR, which validates the effectiveness of the weighted strategy in the tensor sparsity modeling.

2) Parameter Setting: The number of bands B and nonlocal cubics K are two important parameters in the proposed method. In Fig. 12, we show the changes of the PSNR in CAVE with the different numbers of B and K, respectively. From Fig. 12(a), we can observe that denoising results become gradually better with a larger number of bands. It is worth noting that the curve still grows up slowly in the end. Normally, for a $512 \times 512 \times 31$ images, it would cost about 23 min with MATLAB 2017a, on an Intel i7 CPU at 3.6 GHz, and 32-GB memory.

From Fig. 12(b), we can observe that the denoising results become gradually better with a larger number of bands. When the number of the band is smaller than 100, the PSNR value

Authorized licensed use limited to: XIDIAN UNIVERSITY. Downloaded on August 13,2026 at 11:06:50 UTC from IEEE Xplore. Restrictions apply.

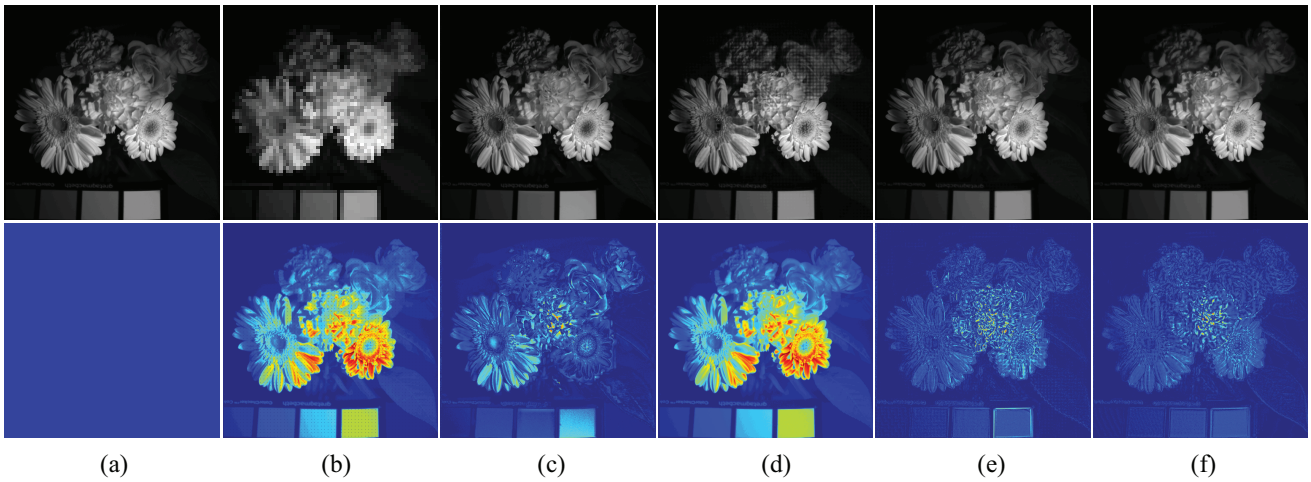


Fig. 10. Simulated SR results on the CAVE dataset. The first row shows the SR results. The second row is the corresponding error map. From the first column to the last one is (a) original image at band 700 nm, (b) low-resolution image ($s = 8$, 8*8, sigma = 3), SR results by (c) CNMF, (d) NLSTF, (e) NSSR, and (f) SR-WLRTR.

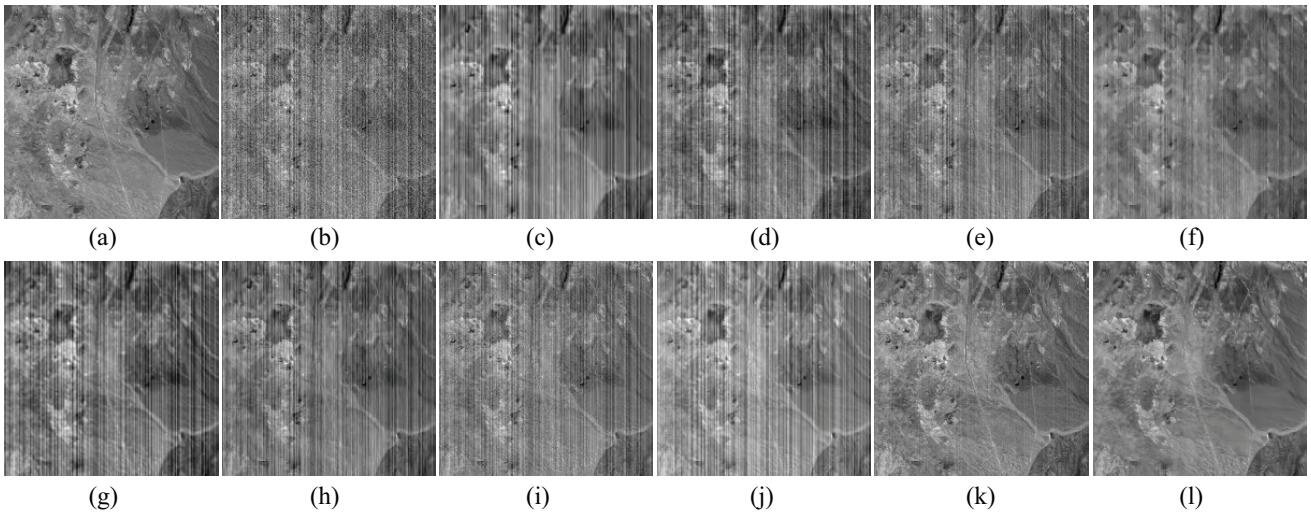


Fig. 11. Simulated mixed noise removal results under extremely heavy mixed random and stripe noise on the *Cuprite* dataset. (a) Original image. (b) Noisy image. Denoising results by (c) BM3D, (d) PARAFAC, (e) LRMR, (f) ANLM, (g) NMF, (h) BM4D, (i) TDL, (j) ITSReg, (k) NMoG, and (l) WLRTR-RPCA.

TABLE IV
QUANTITATIVE RESULTS OF THE COMPETING METHODS UNDER MIXED NOISES

	Salinas(512*217*20)				Cuprite(200*200*89)			
Method	PSNR	SSIM	ERGAS	SAM	PSNR	SSIM	ERGAS	SAM
Noisy	21.57	0.2706	185.21	0.1787	18.84	0.3616	258.22	0.1798
BM3D	29.16	0.7468	50.93	0.0288	20.65	0.3465	183.74	0.1341
PARAFAC	31.25	0.8220	66.52	0.0291	20.99	0.4110	178.00	0.1298
LRMR	35.28	0.8755	41.79	0.0276	21.63	0.5239	140.65	0.1157
ANLM	33.99	0.8704	42.40	0.0278	25.12	0.6259	102.21	0.0717
NMF	29.11	0.6781	35.30	0.0204	21.87	0.4383	165.51	0.1233
BM4D	36.18	0.9155	32.44	0.0198	21.66	0.4641	168.29	0.1255
TDL	38.80	0.9526	26.81	0.0117	21.52	0.4989	170.07	0.1271
ITSReg	33.32	0.8551	32.14	0.0234	21.45	0.4576	175.19	0.1313
NMoG	34.47	0.8773	38.64	0.0226	31.73	0.9178	120.54	0.1121
WLRT-RPCA	**39.38**	**0.9594**	**23.30**	**0.0104**	**33.42**	**0.9319**	**75.74**	**0.0581**

increases extremely fast. After the number of the band is larger than 100, the growing speed of the curve becomes relatively slow, and the PSNR value achieves its highest between 150 and 200. When the number of the band is larger than 230, the performance of WLRTR even deteriorates a little. We suppose it is due to the insufficient similarity between the target cubic and the searching ones. Therefore, in this article, we set the number of nonlocal similarity cubics between 100 and 200.

3) Extension to Multispectral Image: Although WLRTR is proposed for HSIs which possess dozens or hundreds of continuous bands, it can be extended to multispectral images with fewer bands such as RGB color image. Most of the previous color image processing methods usually handle the RGB images in luminance space only or restore each channel separately, while ignoring the spectral correlation across the channel. On the contrary, the WLRTR jointly processes the *R*, *G*, and *B* channels. We compared WLRTR with WNNM [71] which handles the color image in each channel and color image denoising methods: LSCD [84] and CBM3D [85]. The PSNR and SSIM values on BSD are reported in Table VI. We can conclude that the joint utilization of RGB in the color image really improves the denoising performance.

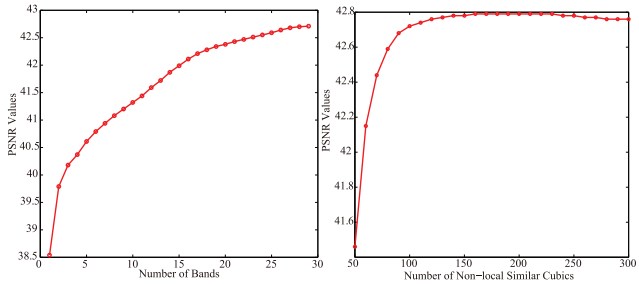
VI. CONCLUSION

In this article, we have proposed a unified WLRTR method for HSI restoration. The proposed WLRTR explicitly utilizes the spatial sparsity, nonlocal spatial-spectral cubic redundancy,

Authorized licensed use limited to: XIDIAN UNIVERSITY. Downloaded on August 13,2026 at 11:06:50 UTC from IEEE Xplore. Restrictions apply.

TABLE V
EFFECTIVENESS ANALYSIS OF WEIGHTED STRATEGY FOR DIFFERENT HSI RESTORATION TASKS

Method	Index	Denoising	Inpainting	Deblurring	SR
Noisy	PSNR	22.10	12.13	25.46	–
	SSIM	0.2352	0.3770	0.8051	–
	ERGAS	324.91	1028.50	225.83	–
	SAM	0.9336	1.1189	0.0877	–
LRTR	PSNR	42.61	43.75	53.83	40.25
	SSIM	0.9795	0.9941	0.9984	0.9854
	ERGAS	30.22	27.42	8.47	50.32
	SAM	0.1161	0.0623	0.0260	0.1018
WLRTR	PSNR	42.81	44.31	55.39	40.47
	SSIM	0.9817	0.9945	0.9989	0.9856
	ERGAS	29.84	25.79	6.97	48.60
	SAM	0.1110	0.0620	0.0228	0.1002



(a) (b)

Fig. 12. Effects of the numbers of bands and nonlocal cubics.

TABLE VI
QUANTITATIVE RESULTS OF DIFFERENT METHODS UNDER SEVERAL NOISE LEVELS ON BSD

Sigma	Index	Methods			
		Noisy	LSCD	CBM3D	WLRTR
10	PSNR	28.13	33.85	35.90	**35.91**
	SSIM	0.7020	0.9188	0.9501	**0.9511**
20	PSNR	22.17	30.26	31.85	**31.94**
	SSIM	0.4580	0.8469	0.8923	**0.8953**
30	PSNR	18.58	28.22	29.69	**29.87**
	SSIM	0.3223	0.7854	0.8402	**0.8444**
40	PSNR	16.08	27.00	28.10	**28.47**
	SSIM	0.2388	0.7417	0.7872	**0.7973**

and spectral consistency via higher order low-rank property of each constructed third-order tensor. We overcome the barriers of classical HSIs restoration methods that are not able to preserve the correlation of the spatial-spectral structure and can only be applied to one specific task. On the one hand, we reveal the fact that the tensor-based sparsity model indeed fits for the HSIs processing; on the other hand, thanks to the variable splitting methods, we show that various HSIs restoration problems can be unified in a framework and transformed into several easier subproblems with a closed-form solution. Furthermore, for the low-rank tensor prior to the related subproblem, we introduce the weighted strategy to improve the restoration performance in which the closed-form solutions have been analyzed. Besides, we consider the very common stripe noise in HSIs, utilize its structural and directional property, and extend WLRTR to the WLRTR-RPCA model.

Extensive simulated and real experimental results have been carried out against several state-of-the-art methods on various HSIs restoration tasks. The proposed methods have consistently outperformed state-of-the-art methods in both quantitative assessments and visual appearance, especially in HSI destriping, deblurring, and super-resolution domain, where few tensor-based methods have been proposed. In the future, we would like to incorporate the learning-based tensor prior [86], [87] into the optimization model for better HSI restoration.

REFERENCES

[1] B. Du and L. Zhang, "A discriminative metric learning based anomaly detection method," *IEEE Trans. Geosci. Remote Sens.*, vol. 52, no. 11, pp. 6844–6857, Nov. 2014.
[2] R. Ji, Y. Gao, R. Hong, Q. Liu, D. Tao, and X. Li, "Spectral–spatial constraint hyperspectral image classification," *IEEE Trans. Geosci. Remote Sens.*, vol. 52, no. 3, pp. 1811–1824, Mar. 2014.
[3] M. Elad and M. Aharon, "Image denoising via sparse and redundant representations over learned dictionaries," *IEEE Trans. Image Process.*, vol. 15, no. 12, pp. 3736–3745, Dec. 2006.
[4] H. Othman and S.-E. Qian, "Noise reduction of hyperspectral imagery using hybrid spatial–spectral derivative-domain wavelet shrinkage," *IEEE Trans. Geosci. Remote Sens.*, vol. 44, no. 2, pp. 397–408, Feb. 2006.
[5] W. Dong *et al.*, "Hyperspectral image super-resolution via non-negative structured sparse representation," *IEEE Trans. Image Process.*, vol. 25, no. 5, pp. 2337–2352, May 2016.
[6] Q. Wei, J. Bioucas-Dias, N. Dobigeon, and J.-Y. Tourneret, "Hyperspectral and multispectral image fusion based on a sparse representation," *IEEE Trans. Geosci. Remote Sens.*, vol. 53, no. 7, pp. 3658–3668, Jul. 2015.
[7] N. Akhtar, F. Shafait, and A. S. Mian, "Sparse spatio-spectral representation for hyperspectral image super-resolution," in *Proc. Eur. Conf. Comput. Vis. (ECCV)*, 2014, pp. 63–78.
[8] Q. Yuan, L. Zhang, and H. Shen, "Hyperspectral image denoising employing a spectral–spatial adaptive total variation model," *IEEE Trans. Geosci. Remote Sens.*, vol. 50, no. 10, pp. 3660–3677, Oct. 2012.
[9] J. Wright, A. Ganesh, S. R. Rao, Y. Peng, and Y. Ma, "Robust principal component analysis: Exact recovery of corrupted low-rank matrices via convex optimization," in *Proc. Neural Inf. Process. Syst. (NIPS)*, 2009, pp. 2080–2088.
[10] H. Zhang, W. He, L. Zhang, H. Shen, and Q. Yuan, "Hyperspectral image restoration using low-rank matrix recovery," *IEEE Trans. Geosci. Remote Sens.*, vol. 52, no. 8, pp. 4729–4743, Aug. 2014.
[11] Y.-Q. Zhao and J. Yang, "Hyperspectral image denoising via sparse representation and low-rank constraint," *IEEE Trans. Geosci. Remote Sens.*, vol. 53, no. 1, pp. 296–308, Jan. 2015.
[12] Y. Xie, Y. Qu, D. Tao, W. Wu, Q. Yuan, and W. Zhang, "Hyperspectral image restoration via iteratively regularized weighted Schatten-norm minimization," *IEEE Trans. Geosci. Remote Sens.*, vol. 54, no. 8, pp. 4642–4659, Aug. 2016.
[13] Y. Xie, S. Gu, Y. Liu, W. Zuo, W. Zhang, and L. Zhang, "Weighted Schatten p-norm minimization for image denoising and background subtraction," *IEEE Trans. Image Process.*, vol. 25, no. 10, pp. 4842–4857, Aug. 2016.
[14] W. He, H. Zhang, L. Zhang, and H. Shen, "Total-variation-regularized low-rank matrix factorization for hyperspectral image restoration," *IEEE Trans. Geosci. Remote Sens.*, vol. 54, no. 1, pp. 178–188, Jan. 2016.
[15] Y. Chen, X. Cao, Q. Zhao, D. Meng, and Z. Xu, "Denoising hyperspectral image with non-IID noise structure," *IEEE Trans. Cybern.*, vol. 48, no. 3, pp. 1054–1066, Mar. 2018.
[16] M. A. Veganzones, M. Simoes, G. Licciardi, N. Yokoya, J. M. Bioucas-Dias, and J. Chanussot, "Hyperspectral super-resolution of locally low rank images from complementary multisource data," *IEEE Trans. Image Process.*, vol. 25, no. 1, pp. 274–288, Jan. 2016.
[17] Y. Chang, L. Yan, T. Wu, and S. Zhong, "Remote sensing image stripe noise removal: From image decomposition perspective," *IEEE Trans. Geosci. Remote Sens.*, vol. 54, no. 12, pp. 7018–7031, Dec. 2016.
[18] L. Zhuang and J. M. Bioucas-Dias, "Fast HSI denoising and inpainting based on low-rank and sparse representations," *IEEE J. Sel. Topics Appl. Earth Observ. Remote Sens.*, vol. 11, no. 3, pp. 730–742, Mar. 2018.
[19] L. D. Lathauwer, B. D. Moor, and J. Vandewalle, "A multilinear singular value decomposition," *SIAM J. Matrix Anal. Appl.*, vol. 21, no. 4, pp. 1253–1278, 2000.

Authorized licensed use limited to: XIDIAN UNIVERSITY. Downloaded on August 13,2026 at 11:06:50 UTC from IEEE Xplore. Restrictions apply.

[20] D. Letexier and S. Bourennane, "Noise removal from hyperspectral images by multidimensional filtering," *IEEE Trans. Geosci. Remote Sens.*, vol. 46, no. 7, pp. 2061–2069, Jul. 2008.

[21] X. Liu, S. Bourennane, and C. Fossati, "Denoising of HSIS using the PARAFAC model and statistical performance analysis," *IEEE Trans. Geosci. Remote Sens.*, vol. 50, no. 10, pp. 3717–3724, Oct. 2012.

[22] X. Guo, X. Huang, L. Zhang, and L. Zhang, "Hyperspectral image noise reduction based on rank-1 tensor decomposition," *ISPRS J. Photogrammetry Remote Sens.*, vol. 83, pp. 50–63, Sep. 2013.

[23] Y. Peng, D. Meng, Z. Xu, C. Gao, Y. Yang, and B. Zhang, "Decomposable nonlocal tensor dictionary learning for multispectral image denoising," in *Proc. IEEE Conf. Comput. Vis. Pattern Recognit. (CVPR)*, 2014, pp. 2949–2956.

[24] W. Dong, G. Li, G. Shi, X. Li, and Y. Ma, "Low-rank tensor approximation with Laplacian scale mixture modeling for multiframe image denoising," in *Proc. IEEE Int. Conf. Comput. Vis. (ICCV)*, 2015, pp. 442–449.

[25] Q. Xie *et al.*, "Multispectral images denoising by intrinsic tensor sparsity regularization," in *Proc. IEEE Conf. Comput. Vis. Pattern Recognit. (CVPR)*, 2016, pp. 1692–1700.

[26] H. Fan, Y. Chen, Y. Guo, H. Zhang, and G. Kuang, "Hyperspectral image restoration using low-rank tensor recovery," *IEEE J. Sel. Topics Appl. Earth Observ. Remote Sens.*, vol. 10, no. 10, pp. 4589–4604, Oct. 2017.

[27] Y. Chang, L. Yan, and S. Zhong, "Hyper-Laplacian regularized unidirectional low-rank tensor recovery for multispectral image denoising," in *Proc. IEEE Conf. Comput. Vis. Pattern Recognit. (CVPR)*, 2017, pp. 4260–4268.

[28] X. Zhang, X. Yuan, and L. Carin, "Nonlocal low-rank tensor factor analysis for image restoration," in *Proc. IEEE Conf. Comput. Vis. Pattern Recognit. (CVPR)*, 2018, pp. 8232–8241.

[29] T. Yokota, B. Erem, S. Guler, S. K. Warfield, and H. Hontani, "Missing slice recovery for tensors using a low-rank model in embedded space," in *Proc. IEEE Conf. Comput. Vis. Pattern Recognit. (CVPR)*, 2018, pp. 8251–8259.

[30] W. He, Q. Yao, C. Li, N. Yokoya, and Q. Zhao, "Non-local meets global: An integrated paradigm for hyperspectral denoising," in *Proc. IEEE Conf. Comput. Vis. Pattern Recognit. (CVPR)*, 2019, pp. 6868–6877.

[31] Q. Xie, M. Zhou, Q. Zhao, D. Meng, W. Zuo, and Z. Xu, "Multispectral and hyperspectral image fusion by MS/HS fusion net," in *Proc. IEEE Conf. Comput. Vis. Pattern Recognit. (CVPR)*, 2019, pp. 1585–1594.

[32] R. Dian, L. Fang, and S. Li, "Hyperspectral image super-resolution via non-local sparse tensor factorization," in *Proc. IEEE Conf. Comput. Vis. Pattern Recognit. (CVPR)*, 2017, pp. 5344–5353.

[33] S. Gu, L. Zhang, W. Zuo, and X. Feng, "Weighted nuclear norm minimization with application to image denoising," in *Proc. IEEE Conf. Comput. Vis. Pattern Recognit. (CVPR)*, 2014, pp. 2862–2869.

[34] R. Yan, L. Shao, and Y. Liu, "Nonlocal hierarchical dictionary learning using wavelets for image denoising," *IEEE Trans. Image Process.*, vol. 22, no. 12, pp. 4689–4698, Dec. 2013.

[35] L. Zhang, W. Wei, Y. Zhang, C. Shen, A. van den Hengel, and Q. Shi, "Cluster sparsity field for hyperspectral imagery denoising," in *Proc. Eur. Conf. Comput. Vis. (ECCV)*, 2016, pp. 631–647.

[36] Y. Fu and W. Dong, "3D magnetic resonance image denoising using low-rank tensor approximation," *Neurocomputing*, vol. 195, pp. 30–39, Jun. 2016.

[37] Y. Fu, A. Lam, I. Sato, and Y. Sato, "Adaptive spatial–spectral dictionary learning for hyperspectral image restoration," *Int. J. Comput. Vis.*, vol. 122, no. 2, pp. 228–245, 2017.

[38] X. Cao *et al.*, "Low-rank matrix factorization under general mixture noise distributions," in *Proc. IEEE Conf. IEEE Int. Conf. Comput. Vis. (ICCV)*, 2015, pp. 1493–1501.

[39] M. Maggioni, V. Katkovnik, K. Egiazarian, and A. Foi, "Nonlocal transform-domain filter for volumetric data denoising and reconstruction," *IEEE Trans. Image Process.*, vol. 22, no. 1, pp. 119–133, Jan. 2013.

[40] A. Rajwade, A. Rangarajan, and A. Banerjee, "Image denoising using the higher order singular value decomposition," *IEEE Trans. Pattern Anal. Mach. Intell.*, vol. 35, no. 4, pp. 849–862, Apr. 2013.

[41] H. Shen and L. Zhang, "A map-based algorithm for destriping and inpainting of remotely sensed images," *IEEE Trans. Geosci. Remote Sens.*, vol. 47, no. 5, pp. 1492–1502, May 2009.

[42] M. Bouali and S. Ladjal, "Toward optimal destriping of modis data using a unidirectional variational model," *IEEE Trans. Geosci. Remote Sens.*, vol. 49, no. 8, pp. 2924–2935, Aug. 2011.

[43] Y. Chang, L. Yan, H. Fang, and C. Luo, "Anisotropic spectral–spatial total variation model for multispectral remote sensing image destriping," *IEEE Trans. Image Process.*, vol. 24, no. 6, pp. 1852–1866, Jun. 2015.

[44] X. Lu, Y. Wang, and Y. Yuan, "Graph-regularized low-rank representation for destriping of hyperspectral images," *IEEE Trans. Geosci. Remote Sens.*, vol. 51, no. 7, pp. 4009–4018, Jul. 2013.

[45] D. Meng and F. De La Torre, "Robust matrix factorization with unknown noise," in *Proc. IEEE Conf. IEEE Int. Conf. Comput. Vis. (ICCV)*, 2013, pp. 1337–1344.

[46] H. Carfantan and J. Idier, "Statistical linear destriping of satellite-based pushbroom-type images," *IEEE Trans. Geosci. Remote Sens.*, vol. 48, no. 4, pp. 1860–1871, Apr. 2010.

[47] J. Fehrenbach, P. Weiss, and C. Lorenzo, "Variational algorithms to remove stationary noise: Applications to microscopy imaging," *IEEE Trans. Image Process.*, vol. 21, no. 10, pp. 4420–4430, Oct. 2012.

[48] X. Liu, X. Lu, H. Shen, Q. Yuan, Y. Jiao, and L. Zhang, "Stripe noise separation and removal in remote sensing images by consideration of the global sparsity and local variational properties," *IEEE Trans. Geosci. Remote Sens.*, vol. 54, no. 1, pp. 3049–3060, May 2016.

[49] C. Lu, J. Feng, Y. Chen, W. Liu, Z. Lin, and S. Yan, "Tensor robust principal component analysis: Exact recovery of corrupted low-rank tensors via convex optimization," in *Proc. IEEE Conf. Comput. Vis. Pattern Recognit. (CVPR)*, 2016, pp. 5249–5257.

[50] Y. Wang, J. Peng, Q. Zhao, Y. Leung, X.-L. Zhao, and D. Meng, "Hyperspectral image restoration via total variation regularized low-rank tensor decomposition," *IEEE J. Sel. Topics Appl. Earth Observ. Remote Sens.*, vol. 11, no. 4, pp. 1227–1243, Apr. 2018.

[51] A. Levin, Y. Weiss, F. Durand, and W. T. Freeman, "Understanding and evaluating blind deconvolution algorithms," in *Proc. IEEE Conf. Comput. Vis. Pattern Recognit. (CVPR)*, 2009, pp. 1964–1971.

[52] H. Shen, L. Du, L. Zhang, and W. Gong, "A blind restoration method for remote sensing images," *IEEE Geosci. Remote Sens. Lett.*, vol. 9, no. 6, pp. 1137–1141, Nov. 2012.

[53] X.-L. Zhao, F. Wang, T.-Z. Huang, M. K. Ng, and R. J. Plemmons, "Deblurring and sparse unmixing for hyperspectral images," *IEEE Trans. Geosci. Remote Sens.*, vol. 51, no. 7, pp. 4045–4058, Jul. 2013.

[54] P. Zhong, N. Peng, and R. Wang, "Learning to diversify patch-based priors for remote sensing image restoration," *IEEE J. Sel. Topics Appl. Earth Observ. Remote Sens.*, vol. 8, no. 11, pp. 5225–5245, Nov. 2015.

[55] S. Henrot, C. Soussen, and D. Brie, "Fast positive deconvolution of hyperspectral images," *IEEE Trans. Image Process.*, vol. 22, no. 2, pp. 828–833, Feb. 2013.

[56] H. Fang, C. Luo, G. Zhou, and X. Wang, "Hyperspectral image deconvolution with a spectral–spatial total variation regularization," *Can. J. Remote Sens.*, vol. 43, no. 4, pp. 384–395, 2017.

[57] Y. Jiang, X. Ding, D. Zeng, Y. Huang, and J. Paisley, "PAN-sharpening with a hyper-Laplacian penalty," in *Proc. IEEE Conf. Comput. Vis. Pattern Recognit. (CVPR)*, 2015, pp. 540–548.

[58] S. Li, H. Yin, and L. Fang, "Remote sensing image fusion via sparse representations over learned dictionaries," *IEEE Trans. Geosci. Remote Sens.*, vol. 51, no. 9, pp. 4779–4789, Sep. 2013.

[59] C. Chen, Y. Li, W. Liu, and J. Huang, "Image fusion with local spectral consistency and dynamic gradient sparsity," in *Proc. IEEE Conf. Comput. Vis. Pattern Recognit. (CVPR)*, 2014, pp. 2760–2765.

[60] N. Akhtar, F. Shafait, and A. Mian, "Bayesian sparse representation for hyperspectral image super resolution," in *Proc. IEEE Conf. Comput. Vis. Pattern Recognit. (CVPR)*, 2015, pp. 3631–3640.

[61] N. Yokoya, T. Yairi, and A. Iwasaki, "Coupled nonnegative matrix factorization unmixing for hyperspectral and multispectral data fusion," *IEEE Trans. Geosci. Remote Sens.*, vol. 50, no. 2, pp. 528–537, Feb. 2012.

[62] R. Kawakami, Y. Matsushita, J. Wright, M. Ben-Ezra, Y.-W. Tai, and K. Ikeuchi, "High-resolution hyperspectral imaging via matrix factorization," in *Proc. IEEE Conf. Comput. Vis. Pattern Recognit. (CVPR)*, 2011, pp. 2329–2336.

[63] E. Wycoff, T.-H. Chan, K. Jia, W.-K. Ma, and Y. Ma, "A non-negative sparse promoting algorithm for high resolution hyperspectral imaging," in *Proc. IEEE Int. Conf. Acoust. Speech Signal Process. (ICASSP)*, 2013, pp. 1409–1413.

[64] C. Lanaras, E. Baltsavias, and K. Schindler, "Hyperspectral super-resolution by coupled spectral unmixing," in *Proc. IEEE Int. Conf. Comput. Vis. (ICCV)*, 2015, pp. 3586–3594.

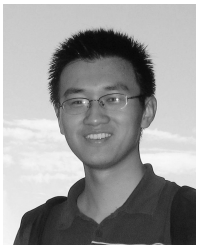
[65] J. Yang, J. Wright, T. S. Huang, and Y. Ma, "Image super-resolution via sparse representation," *IEEE Trans. Image Process.*, vol. 19, no. 11, pp. 2861–2873, May 2010.

[66] L. Loncan *et al.*, "Hyperspectral pansharpening: A review," *IEEE Geosci. Remote Sens. Mag.*, vol. 3, no. 3, pp. 27–46, Sep. 2015.

[67] T. G. Kolda and B. W. Bader, "Tensor decompositions and applications," *J. SIAM Rev.*, vol. 66, no. 4, pp. 294–310, 2005.

Authorized licensed use limited to: XIDIAN UNIVERSITY. Downloaded on August 13,2026 at 11:06:50 UTC from IEEE Xplore. Restrictions apply.

[68] Z. Lin, R. Liu, and Z. Su, "Linearized alternating direction method with adaptive penalty for low-rank representation," in *Proc. Neural Inf. Process. Syst. (NIPS)*, 2011, pp. 612–620.
[69] E. J. Candes, M. B. Wakin, and S. P. Boyd, "Enhancing sparsity by reweighted L_1 minimization," *J. Fourier Anal. Appl.*, vol. 14, no. 5, pp. 877–905, 2008.
[70] L. Mirsky, "A trace inequality of John von Neumann," *Monatshefte für mathematik*, vol. 79, no. 4, pp. 303–306, 1975.
[71] S. Gu, Q. Xie, D. Meng, W. Zuo, X. Feng, and L. Zhang, "Weighted nuclear norm minimization and its applications to low level vision," *Int. J. Comput. Vis.*, vol. 121, pp. 1–26, Jul. 2016.
[72] S. Chrétien and T. Wei, "Von Neumann's trace inequality for tensors," *Linear Algebra Appl.*, vol. 482, pp. 149–157, Oct. 2015.
[73] L. De Lathauwer, "Decompositions of a higher-order tensor in block terms—Part II: Definitions and uniqueness," *SIAM J. Matrix Anal. Appl.*, vol. 30, no. 3, pp. 1033–1066, 2008.
[74] C.-F. Chen, C.-P. Wei, and Y.-C. F. Wang, "Low-rank matrix recovery with structural incoherence for robust face recognition," in *Proc. IEEE Conf. Comput. Vis. Pattern Recognit. (CVPR)*, 2012, pp. 2618–2625.
[75] G. Liu, Z. Lin, S. Yan, J. Sun, Y. Yu, and Y. Ma, "Robust recovery of subspace structures by low-rank representation," *IEEE Trans. Pattern Anal. Mach. Intell.*, vol. 35, no. 1, pp. 171–184, Jan. 2013.
[76] R. Bracewell and P. B. Kahn, "The Fourier transform and its applications," *Amer. J. Phys.*, vol. 34, no. 8, p. 712, 1966.
[77] A. Chakrabarti and T. Zickler, "Statistics of real-world hyperspectral images," in *Proc. IEEE Conf. Comput. Vis. Pattern Recognit. (CVPR)*, 2011, pp. 193–200.
[78] K. Dabov, A. Foi, V. Katkovnik, and K. Egiazarian, "Image denoising by sparse 3-D transform-domain collaborative filtering," *IEEE Trans. Image Process.*, vol. 16, no. 8, pp. 2080–2095, Aug. 2007.
[79] N. Renard, S. Bourennane, and J. Blanc-Talon, "Denoising and dimensionality reduction using multilinear tools for hyperspectral images," *IEEE Geosci. Remote Sens. Lett.*, vol. 5, no. 2, pp. 138–142, Apr. 2008.
[80] J. V. Manjón, P. Coupé, L. Martí-Bonmatí, D. L. Collins, and M. Robles, "Adaptive non-local means denoising of MR images with spatially varying noise levels," *J. Magn. Resonance Imag.*, vol. 31, no. 1, pp. 192–203, 2010.
[81] M. Ye, Y. Qian, and J. Zhou, "Multitask sparse nonnegative matrix factorization for joint spectral–spatial hyperspectral imagery denoising," *IEEE Trans. Geosci. Remote Sens.*, vol. 53, no. 5, pp. 2621–2639, May 2015.
[82] D. Krishnan and R. Fergus, "Fast image deconvolution using hyper-Laplacian priors," in *Proc. Neural Inf. Process. Syst. (NIPS)*, 2009, pp. 1033–1041.
[83] S. Pyatykh, J. Hesser, and L. Zheng, "Image noise level estimation by principal component analysis," *IEEE Trans. Image Process.*, vol. 22, no. 2, pp. 687–699, Feb. 2013.
[84] M. Rizkinia, T. Baba, K. Shirai, and M. Okuda, "Local spectral component decomposition for multi-channel image denoising," *IEEE Trans. Image Process.*, vol. 25, no. 7, pp. 3208–3218, Jul. 2016.
[85] K. Dabov, A. Foi, V. Katkovnik, and K. Egiazarian, "Color image denoising via sparse 3D collaborative filtering with grouping constraint in luminance-chrominance space," in *Proc. IEEE Int. Conf. Image Process. (ICIP)*, 2007, pp. 310–313.
[86] Y. Chang, L. Yan, H. Fang, S. Zhong, and W. Liao, "HSI-DeNet: Hyperspectral image restoration via convolutional neural network," *IEEE Trans. Geosci. Remote Sens.*, vol. 57, no. 2, pp. 667–682, Feb. 2019.
[87] Q. Yuan, Q. Zhang, J. Li, H. Shen, and L. Zhang, "Hyperspectral image denoising employing a spatial–spectral deep residual convolutional neural network," *IEEE Trans. Geosci. Remote Sens.*, vol. 57, no. 2, pp. 1205–1218, Feb. 2019.



Yi Chang (Student Member, IEEE) received the B.S. degree in automation from the University of Electronic Science and Technology of China, Chengdu, China, in 2011, and the M.S. and Ph.D. degrees from the School of Artificial Intelligence and Automation, Huazhong University of Science and Technology, Wuhan, China, in 2014 and 2020, respectively.

From 2014 to 2015, he was a Research Assistant with Peking University, Beijing, China. He was a Research Intern with Tencent Youtu Lab, Shanghai, China. He is currently a Postdoctoral Fellow with the AI Center, Peng Cheng Lab, Shenzhen, China. His research interests include image processing and computer vision.



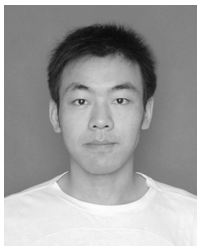
Luxin Yan (Member, IEEE) received the B.S. degree in electronic communication engineering and the Ph.D. degree in pattern recognition and intelligence systems from the Huazhong University of Science and Technology (HUST), Wuhan, China, in 2001 and 2007, respectively.

He is currently a Professor with the School of Artificial Intelligence and Automation, HUST. His research interests include multispectral image processing, pattern recognition, and real-time embedded systems.



Xi-Le Zhao received the M.S. and Ph.D. degrees from the University of Electronic Science and Technology of China (UESTC), Chengdu, China, in 2009 and 2012, respectively.

He is currently a Professor with the School of Mathematical Sciences, UESTC. His main research interests focus on the models and algorithms of high-dimensional image processing problems.



Houzhang Fang received the M.S. and Ph.D. degrees in applied mathematics and control science from the Huazhong University of Science and Technology, Wuhan, China, in 2010 and 2014, respectively.

He is currently a Lecturer with Xidian University, Xi'an, China. His research interests include image restoration, blind image deconvolution, object detection, and recognition.



Zhijun Zhang received the bachelor's degree from the School of Life Science and Technology, Huazhong University of Science and Technology, Wuhan, China, in 2015. She is currently pursuing the Ph.D. degree with the School of Artificial Intelligence and Automation advised by Prof. Sheng Zhong.

From 2019 to 2020, she has been a Visiting Pre-Doctoral Fellow with the Northwestern University under the supervision of Prof. Ying Wu. Her research interests focus on the computer vision and deep learning with video analysis and understanding, action detection, and reasoning.



Sheng Zhong received the Ph.D. degree in pattern recognition and intelligent systems from the Huazhong University of Science and Technology (HUST), Wuhan, China, in 2005.

He is currently a Professor with the School of Artificial Intelligence and Automation, HUST. His research interests are pattern recognition, image processing, and real-time embedded system.

Authorized licensed use limited to: XIDIAN UNIVERSITY. Downloaded on August 13,2026 at 11:06:50 UTC from IEEE Xplore. Restrictions apply.